# CHALCOGENIDE GLASS FIBER TAPERS FOR MIR SUPERCONTINUUM GENERATION

by

SOROUSH SHABAHANG
B.S. in Physics: Kharazmi University, Iran; summer 2004
M.S. in Optics: Shahid Beheshti University, Iran; spring 2008

A dissertation submitted in partial fulfillment of the requirements
for the degree of Doctor of Philosophy
in CREOL, the College of Optics & Photonics
at the University of Central Florida
Orlando, Florida

Spring Term
2014

Major Professor: Ayman Abouraddy

# ABSTRACT

The development of optical sources and components suitable for the mid-infrared is crucial for applications in this spectral range to reach the maturity level of their counterparts in the visible and near-infrared spectral regimes. The recent commercialization of quantum cascade lasers is leading to further interest in this spectral range. Wideband mid-infrared coherent sources, such as supercontinuum generation, have yet to be fully developed. A mid-infrared supercontinuum source would allow for unique applications in spectroscopy and sensing.

Over the last decade, it has been shown that high-index confinement in highly nonlinear fibers pumped with high-peak-power pulses is an excellent approach to supercontinuum generation in the visible and near-infrared. Nonlinear waveguides such as fibers offer an obvious advantage in increasing the nonlinear interaction length maintained with a small cross section. In addition, fiber systems do not require optical alignment and are mechanically stable and robust with respect to the environmental changes. These properties have made fiber systems unique in applications where they are implemented in a harsh and unstable environment.

In extending this approach into the mid-infrared, I have used chalcogenide glass fibers. Chalcogenide glasses have several attractive features for this application: they have high refractive indices for high optical-confinement, have a wide transparency window in the mid-infrared, and have a few orders-of-magnitude higher nonlinearity than silica glass and other mid-IR glasses. Producing chalcogenide glass fiber tapers offer, furthermore, the possibility of dispersion control and stronger field confinement and hence higher nonlinearity, desired for supercontinuum generation.

Dedicated to Mahsa!

# ACKNOWLEDGMENTS

I would like to express my deepest gratitude to my advisor, Dr. Ayman Abouraddy for guiding my research for the past several years and also for his endless support, caring and patience.

I would also like to thank the committee members, professors Vanstryland, Dogariu and Belfield.

Thanks to Professor Fink and his group at MIT for all the constructive collaborations. Thanks to LPL group for letting me use their Tm fiber laser and also for the loan of equipment. Thanks to Ultrafast group for getting me access to their lasers. Thanks to NLO group for helping us with the Zscan measurements. Also thanks to MIR-combs group for the access to their Tm fiber laser.

Many thanks to my friends in Multi-OFD group. In particular, I would like to thank Hooman, Josh, Guangming and Felix for all their help and useful discussions. My research would not have been possible without their help.

Thanks to Rachel, Richard, Deon, Amy and Gail and all other staff in CREOL for all their help and for making CREOL a good second home for all of us, with many good memories.

Finally, and most importantly, I would like to thank my family and particularly my parents. They were always supporting me and encouraging me with their best wishes.

# TABLE OF CONTENTS

LIST OF FIGURES ..... vi
LIST OF TABLES ..... ix
INTRODUCTION ..... 1
CHAPTER 1 OUR CHALCOGENIDE FIBER AND FIBER TAPERS ..... 5
1.1. Fiber Structure and Fabrication ..... 5
1.2. Mechanical Properties of the Fiber ..... 7
1.3. Fiber Tapering ..... 9
CHAPTER 2 DISPERSION CHARACTERIZATION ..... 16
2.1. Chromatic Dispersion of Chalcogenide Glasses ..... 16
2.2. Measurement Setup and Procedure ..... 18
2.3. Dispersion of Bulk Samples and the Fiber ..... 20
2.4. Dispersion of Fiber Samples ..... 21
2.5. Dispersion of Nanotaper Samples ..... 22
2.6. Designs for all-solid zero-GVD ChG fibers ..... 24
CHAPTER 3 NONLINEAR CHARACTERIZATION OF NANOTAPERS ..... 25
3.1. Nonlinearity in Chalcogenide Glasses ..... 25
3.2. Nonlinear Characterization of Bulk Chalcogenides ..... 27
3.3. Nonlinear Characterization of Robust Composite ChG nanotapers ..... 28
3.3.1. Nanotaper Samples ..... 28
3.3.2. Nonlinear Characterization Methodology ..... 31
3.3.3. Self-phase modulation (SPM) measurements ..... 32
3.4. Supercontinuum Generation (SCG) Measurements ..... 33
3.4.1. Pumping at 1.55-μm-Wavelength ..... 34
3.4.2. Pumping at 2-μm-Wavelength ..... 39
CHAPTER 4 PARTICLE FABRICATION BY PLATEAU-RAYLEIGH CAPILLARY INSTABILITY IN MULTI-MATERIAL OPTICAL FIBERS ..... 43
APPENDIX A GLASS FABRICATION AND PREFORM EXTRUSION ..... 49
APPENDIX B ZSCAN MEASUREMENT ..... 51
APPENDIX C SPECTRAL BROADENING SIMULATIONS ..... 53
REFERENCES ..... 56

# LIST OF FIGURES

Fig. 1. (a) FTIR transmission spectra for three ChG samples. G1: As2Se3; G2: As2Se1.5S1.5; and G3: As2S3. Each sample is a 10-mm-diameter disc of thickness ≈ 2 mm. Insets show photographs of the samples; all scale bars are 5 mm. (b) FTIR transmission spectra showing the low-wavelength cutoff for G1, G2, and G3. (c) FTIR transmission spectrum for a 2-mmthick polymer sample; PES: polyethersulfone. ..... 6

Fig. 2. Scanning electron microscope (SEM) images of the fiber (left) full cross section, and (right) ChG core/cladding region. ..... 7

Fig. 3. Tensile-strength measurement for (a) a bare 400-μm-thick chalcogenide fiber and (b) 740-μm-thick PES fiber. ..... 7

Fig. 4. (a) A 1-mm-diameter fiber tied in a 1-in.-diameter knot. (b) Transmission over time for 10 fibers after bending the fiber with 0.5-inch-bend diameter. The black curve is the average of all the measurements. (c) A 2 kg weight hanging from a 5-cm-long fiber. The inset shows the hanging mechanism. The fiber is attached to microscope slides using epoxy while keeping the ends free for optical measurements. (d) A robust multimaterial taper. The inset is a micrograph of the taper center. ..... 8

Fig. 5. Tapering setup. Inset shows the fiber used in the tapering experiments. ..... 10

Fig. 6. Fiber axial plastic deformation upon heating in a tapering setup with 5-mm-wide uniform heating zone – corresponding to the red rectangle in panel (a). Panels (a) through (e) are transmission optical micrographs that correspond to identical samples (equivalent drawing tension of 40 g) at different temperatures for 40 s. Initial fiber outer diameter is 1 mm. (f) Transmission optical micrograph showing a magnified side image of the intact G1 core inside the PES cladding. The black symmetric outer portions of the cladding in the microscope image result from the curvature of the taper outer surface. ..... 11

Fig. 7. Dependence of the axial plastic deformation upon heating in a tapering setup (see Fig. 6) on the tension during fiber drawing and tapering time. Each panel is an optical transmission micrograph of a fiber sample with initial fiber outer diameter 1 mm. The tapering temperature is held fixed throughout and the fiber-drawing tension is constant in each column. ..... 12

Fig. 8. (a) A robust nano-taper with minimum core midway along the sample dcmin = 400 nm. (b) A nano-taper mounted on a glass slide and is fixed using epoxy, after which the facets are polished. (c) SEM micrograph of the nano-taper cross section at the taper mid-point (corresponding to minimum diameter). (d) Higher-magnification SEM micrograph highlighting the ChG core/cladding structure; compare to Fig. 2-b. ..... 13

Fig. 9. (a) Axial profile of the core of a nanotaper with $d_c^{min}$ = 250 nm. (b) Power distribution of fundamental mode in the core, cladding and jacket of the fiber as a function of core diameter, calculated for 1.55 and 2 μm wavelengths. (c) Transmission loss of several tapers with different dcmin, measured at λ=1.55 μm in 25-mm-long tapers – normalized to the transmission in an equal length of non-tapered fiber. ..... 14

Fig. 10. Setup for measuring $\beta_2$. S: source, FC: fiber coupler, C: collimator, L: lens, A: attenuator (to increase fringe visibility), and OSA: optical spectrum analyzer. Solid lines are single-mode fibers. ..... 19

Fig. 11. (a) Spectral interference fringes in the output spectrum $I_o$ (λ) (note the logarithmic vertical scale) obtained using an OSA (Advantest Q8381A). The sample here is the BK7 bulk cube and the source is

amplified spontaneous emission (ASE) from an EDFA (EAU-200-c, IPG Photonics). (b) The Fourier transform (FT) of $I_o$ (λ). The black dashed box corresponds to the portion filtered out to extract the interference fringes. (c) Filtered spectral power density obtained by taking the inverse FT of (b) and the extracted spectral phase Δϕ (λ). (d)-(f) are similar to (a)-(c) except that the source is ASE from a thulium fiber laser, the OSA is Yokogawa AQ6375 and the sample used is a bulk As2S3 disc; see Fig. 1-a, lower-left inset.....20

Fig. 12. (a) Measured diameter profile along the nano-tapers' axes (Table 3). Only half the length of the tapers is shown. The other half of each profile is a mirror reflection around the midpoint. Diameter ranges corresponding to normal and anomalous GVD are identified. (b) Calculated waveguide β2 for Fiber II at λ=1.55 μm and λ=1.95 μm for different core diameters. (c) Calculated waveguide β2 as a function of core diameter and wavelength. The two horizontal dashed lines correspond to the wavelengths used in our measurements.....23

Fig. 13. (a) Closed-aperture and (b) open-aperture (three-photon absorption here) Z-scan results for a $As_2Se_{1.5}S_{1.5}$ sample at different incident femtosecond-pulse energies (see text and Appendix-2 for details). The dots are the measured values and the solid lines are the fitted curves. The inset in (b) is a photograph of the $As_2Se_{1.5}S_{1.5}$ sample.....28

Fig. 14. (a) Longitudinal core diameter dc profiles of the four samples used in the experiments; z is taken along the nanotaper axis. ($d_c^{min}$, L)of Samples through 4 are: (580 nm, 42 mm), (400 nm, 25 mm), (375 nm, 46 mm), and (250 nm, 68 mm), respectively. See also Table 4. (b) The total GVD parameter $\beta_2$ as a function dc calculated at λ=1.55 and 2 μm. (c) The blue curve (left vertical axis) shows the diameter of the fundamental mode dm at λ=1.55 μm, which indicates the optical-mode confinement when compared to dc, and the green curve (right vertical axis) is the nonlinear coefficient γ of the fiber as a function of core diameter dc, calculated for the fundamental mode at λ=1.55 μm. The inset shows the region of the curve of γ that is encircled (dashed circle) and highlights the non-monotonic relationship between $d_m$ and $d_c$ at sub-micrometer core diameters (250 nm<$d_c$<1 μm). The two-dashed vertical lines in the inset correspond to dc=600 nm (where $d_m/d_c$ exceeds 1) and dc=450 nm (where confinement by the polymer jacket starts to dominate). See text for details. .....29

Fig. 15. Setup for nonlinear optical characterizations.....32

Fig. 16. SPM characterization results obtained in two different experiments: (a) picosecond pulses launched into nanotaper Sample 4 and (b) femtosecond pulses launched into nanotaper Sample 2. The power levels are the input peak powers for each sample without corrections for Fresnel reflection from the sample facets. (c) SPM simulation results for the two different experiments shown in (a) and (b): (c) picosecond pulses launched into Sample 4 and (d) femtosecond pulses launched into Sample 2. The power levels are the estimated peak powers in the tapered section of each sample after correcting for Fresnel reflections at the sample facets and nanotaper losses (see text for details).....33

Fig. 17. (a) Schematic of the optical setup: A, attenuator; $L_1$, $L_2$, lenses; T, nanotaper; FC, fiber collimator; SMF, single-mode fiber; OSA, optical spectrum analyzer. (b) Autocorrelation trace, (c) spectrum, and (d) pump mode distribution 2 m from the laser. Since the beam lacks symmetry, the coupling efficiency was reduced compared to a symmetric spatial mode. .....35

Fig. 18. SCG in robust ChG tapers. The measured output spectrum is plotted with increasing input pump power from (i) through (vi).....36

Fig. 19. Calculated spectrum at the nanotaper output with increasing input pump power obtained by integrating the GNLSE. See text for details. (b) Output spectrum for input $P_p$=3, 5, and 10 kW. ..... 37

Fig. 20. (a) Measured and (b) stimulated continuums for samples 1, 2, and 3. The input pulse parameters are 3.5 mW input, 20 MHz, 400 fs. The power levels in the stimulated spectra are estimated for sample 1, 2 and 3 are 1 mW, 0.8 mW, and 0.85 mW, respectively. ..... 38

Fig. 21. (a) Schematic of the optical setup for MIR spectral measurement; shorter wavelengths from visible to 2.4 μm are measured by means of two OSAs, longer wavelengths are modulated by a chopper, routed through a monochromator and measured by a PbSe detector connected to a lock-in amplifier. A long-pass-filter is placed on the beam path to avoid overlapping of the long-wavelengths with the diffracted short-wavelengths in the monochromator. (b) Measured continuum generated from a 6.8-cm-long nanotaper with $d_c^{min}$=250 nm, pumped at 2 μm by 450-fs pulses, with an average power of 250 mW and 58-MHz repetition rate. ..... 40

Fig. 22. Measured continuum generated from a 7-cm-long nanotaper with $d_c^{min}$=400 nm, pumped by sub-100-fs pulses, operating at 80-MHz repetition rate. The dashed lines show the noise level of detector. The spectral measurement was by means of an OSA (up to 1700 nm) and an FTIR and liquid nitrogen detector for longer wavelengths. ..... 41

Fig. 23. (a) Tapering setup. Inset shows the tapering parameters. (b) Optical micrograph of a fiber cross section. Inset shows a magnified image of the core (scale bar is 20 μm). (c) A typical fiber taper side view. (d) Magnified side view image of the taper center (corresponding to the dotted box in (c)) showing the broken core. (e) Optical micrographs of the fiber tapers side view produced at different T ($v$=0.5mm/s and $l$=15 mm) showing different stages of the core breakup driven by the PR capillary instability. (f) Glass viscosity $\mu_g$ as a function of T. ..... 44

Fig. 24. (a)–(d) SEM micrographs of the fiber core at different stages of the PR instability during static heating at 287° C. Scale bars are all 20 μm. (e) Optical micrograph of the fiber after core breakup. (f) A single period corresponding to the dotted box in (e). In order to make the satellites visible, the fiber is squeezed between two microscope slides. (g) Magnified image of the satellites and sub-satellites corresponding to the dotted box in (f). ..... 46

Fig. 25. (a) Dependence of the instability growth time $\tau_B$ on temperature T during static heating. We calculate and plot $\tau_B$ over the same temperature range for D=9, 10, and 11 μm. (b) Calculated instability rate ($1/\tau_B$) as a function of T and x. The black line shows the highest instability rate as a function of temperature, thus identifying $x_m$. (c)–(e) Effect of tapering parameters on core breakup period $P_B$: (c) l, (d) v, and (e) T. Continuous curves are theoretical fits and "+" are data points. (f)–(h) Optical micro-graphs of glass particles with prescribed sizes obtained after dissolving the polymer cladding. Scale bars are all 10 μm. (i)–(k) SEM micrographs of single particles corresponding to (f)–(h), respectively. Scale bars are all 2 μm. ..... 47

# LIST OF TABLES

Table 1. Measured bulk index n and GVD β2 in ps2/km at 1.55 μm and 1.95 μm wavelengths. The indices n are estimated within ±0.015. ..... 21

Table 2. Measured (Meas) and simulated (Sim) fiber GVD $\beta_2$ at 1.55 μm in $ps^2$/km; Jacket: polymer outer jacket. $G_1$, $G_2$ and $G_3$ are defined in table 1. ..... 22

Table 3. Measured (Meas.) and simulated (Sim.) average GVD β2 at 1.55 μm in $ps^2$/km for Fiber-II nano-tapers. ..... 22

Table 4. Nanotaper Sample Parameters; Here dcmin is the minimum core diameter at the nanotaper axial midpoint; L is the nanotaper total length; T is the sample transmission (including the Fresnel reflection at the facets). ..... 30

# INTRODUCTION

Chalcogenide glasses (ChGs) stand out as the only family of optical materials that are transparent across the entire infrared [1] and that may also be stably drawn into extended optical fibers. Moreover, ChGs exhibit higher optical nonlinearities than most rival glasses in the MIR. For example, As2Se3 has approximately one order-of-magnitude higher nonlinear refractive index $n_2$ compared to tellurite glasses and two orders-of-magnitude higher than ZBLAN glasses [2]. A wide range of applications may benefit from these features, such as high-speed optical communication that requires ultra-fast all-optical processing and switching capabilities [3]. The mechanism in basic optical switching devices is typically based on Kerr nonlinearity, whose high value in ChGs has thus made potential candidates for switching devices [4, 5].

Nonlinear waveguides such as fibers offer an obvious advantage in increasing the nonlinear interaction length maintained with a small cross section. For instance, in MIR-supercontinuum generation (SCG), as a broad-band MIR optical source for spectroscopy applications, there are many research focusing on optical fibers made from MIR glasses like tellurite [6, 7], fluoride [8, 9] and chalcogenides [10]. In addition, fiber systems do not require optical alignment and are mechanically stable and robust with respect to the environmental changes. These properties have made fiber systems unique in applications where they are implemented in a harsh and unstable environment.

Although ChG fibers were first demonstrated decades ago, and have since found uses in a wide range of linear and nonlinear infrared applications [11], they were used for SCG only as recently as 2005 [12]. This delay was in large part due to several limitations of ChGs: poor power handling capabilities (due to photodarkening) [13], low damage threshold [14] and high normal group velocity dispersion (GVD) [15]. To obviate these limitations in ChGs and produce broad supercontinuum, novel approaches and fiber designs are then required; for instance: cascaded Raman-frequency shift [11, 16, 17], spectral broadening in dispersion-engineered photonic crystal fibers (PCFs) [12] and

suspended core fiber structures [18], and fiber tapers [19, 20]. In the cascaded Raman method, the sample is pumped with long pulses (typically from tens of picoseconds to nanoseconds) and spectral broadening is due to stimulated Raman scattering (SRS). Cross-phase-modulation (XPM) and self-phase-modulation (SPM) play significant roles in spectral flattening. The long input pulses used eliminate the need for dispersion engineering; a drawback is that the generated continuum is expected to be incoherent [21]. ChG PCFs were first reported in 2006 [22], and have since been used in demonstrating SCG. One advantage of micro-structured ChG fibers (whether PCF or suspended core) is that they enable GVD engineering; allowing for the compensation of the material-GVD [23, 24]. In these arrangements SPM plays a significant role in the spectral broadening. Furthermore, soliton-involved processes and four-wave-mixing may also kick in, depending on the dispersion value at the pump wavelength [21]. Although the first demonstration of SCG in a fiber taper was in 2000 [25], ChG fiber tapers for SCG application were not used until 7 years. Unfortunately, bare ChG fibers were not robust which made handling of ChG tapers extremely difficult. Despite this technical obstacle, the high potential of ChG tapers in nonlinear optics was still motivating. In 2007, an As2Se3 fiber was tapered down to a waist diameter of 1.2 μm [26]. Based on SPM measurements, an enhanced nonlinearity of 62,000× that of standard silica single mode fiber was inferred. After this work, more results have been reported on nonlinear ChG fiber tapers [19, 20, 27, and 28] and microstructured fiber tapers [29]. The broadening mechanism for SCG in fiber tapers is similar to that in micro-structured fibers. The possibility of light confinement in an ultra-small area of fiber tapers significantly enhances optical nonlinearities. In addition, broadband single-mode guidance in tapers results in retaining a uniform spatial profile in the generated SC. Tapering is also a flexible tool for dispersion engineering. By an appropriate choice of core and cladding materials, one can reach to a wide range of chromatic dispersion values simply by changing the tapering ratio [26].

As mentioned earlier, weak mechanical properties and brittleness is the main drawback of the ChG fiber tapers which stems from the fragile nature of soft ChGs. Some composite structures have

so far been suggested in order to improve the robustness and enhance control over dispersion in ChG fibers; for instance: ChG-silica step index fibers [30], ChG-PMMA hybrid-microwires [31, 32], and ChG-Core Tellurite-Cladding microstructured fiber [33]. High material loss of PMMA and silica at long wavelengths represent a drawback in the MIR applications for the first two. Recently, we have developed a new extrusion based technique for fabricating robust ChG fibers by adding a built-in protective polymer jacket to the fiber structure [34]. Since the ChG and polymer are thermally compatible, the drawn fiber may be tapered without removing the polymer jacket. Also due to high relatively high index contrast between the core and cladding, the optical mode is well confined in the core.

Besides my original goal on SCG, the accurate tapering capability brought us the chance to observe the Plateau Raleigh Instability (PRI) for the first time in a solid fiber during fiber tapering, which can be used for fabrication of structured nanoparticles. I have also recently discovered a new phenomenon which can be used for fabricating scalable particles with designable cross-sections. The approach is based on cold-drawing of a polymer fiber or film with a fragile material embedded in or coated on it.

In the first chapter of this thesis I will introduce our fiber structure and the material. Tapering is a key factor in increasing the nonlinear response of fiber at lower optical powers; hence our home-made tapering system is introduced, different tapering parameters to control the taper-profiles are explained and some optical characterizations on the nanotapers are provided. The second chapter is dedicated to investigating the chromatic dispersion; that is because dispersion control is crucial to nonlinear optical applications in optical fibers, such as supercontinuum generation. I introduce my own approach to measuring the dispersion of chalcogenide bulk, fiber, and nanotapers and present the simulation and experimental results. In the third chapter, the results of nonlinear characterizations on the nanotapers, performed by SPM measurement, and also SC results pumped by different optical

sources are presented. Finally in the last chapter, nanoparticle fabrication by the two approaches (PRI and cold-drawing) is explained.

# CHAPTER 1
# OUR CHALCOGENIDE FIBER AND FIBER TAPERS

## 1.1. Fiber Structure and Fabrication

We fabricate step-index chalcogenide glass fibers for optical experiments. Before the fiber fabrication process, we determined the transparency windows of some ChGs which could be used in our fibers using an FTIR spectrometer (Bruker Tensor 37) in the spectral range of 0.5–20 μm. These three ChGs have high third-order optical nonlinearity (will be explained more in the nonlinear characterization section) and their stable thermo-mechanical properties allow for thermal drawing into fibers [35]. The bulk samples of three ChG compositions were prepared: G1 (As2Se3); G2 (As2Se1.5S1.5); and G3 (As2S3) (Fig. 1). The samples were prepared in the form of 2-mm thick and 10-mm-diameter disks; see Fig. 1-a. Details of glass fabrication are explained in Appendix-1. We note the gradual shift of the absorption band edges to longer wavelengths as Se replaces S in the glass matrix at both the long-wavelength [Fig. 1-a] and short-wavelength [Fig. 1-b] ends. In addition, we measured the optical transmission of a typical thermoplastic polymer, polyethersulfone (PES), used in the fibers as a protective jacket; see Fig. 1-c. As is clear, PES is highly absorptive in the MIR. In designing such fibers, care must thus be taken to minimize the fraction of light reaching the polymer.

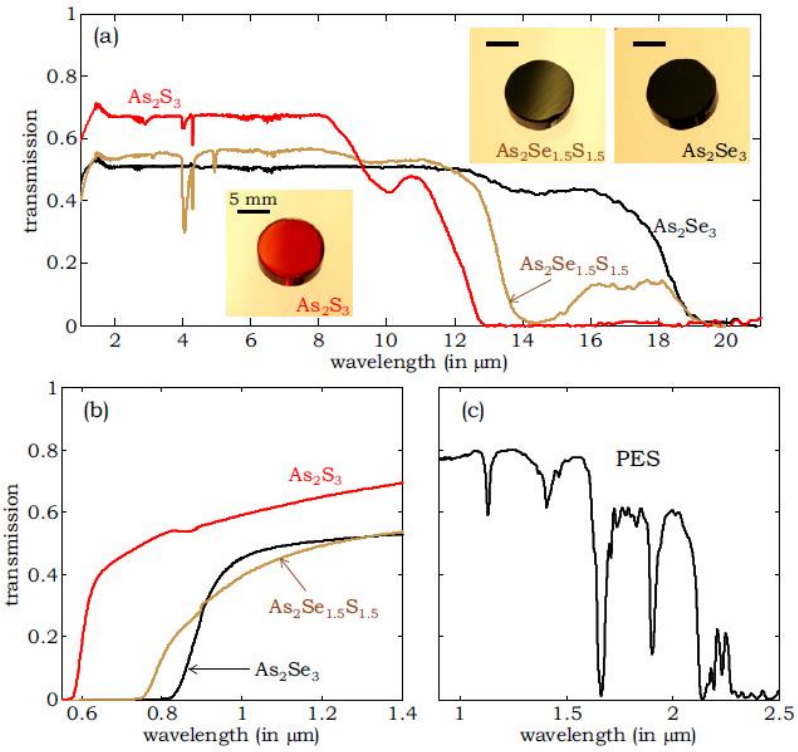


Fig. 1. (a) FTIR transmission spectra for three ChG samples. G1: As2Se3; G2: As2Se1.5S1.5; and G3: As2S3. Each sample is a 10-mm-diameter disc of thickness ≈ 2 mm. Insets show photographs of the samples; all scale bars are 5 mm. (b) FTIR transmission spectra showing the low-wavelength cutoff for G1, G2, and G3. (c) FTIR transmission spectrum for a 2-mmthick polymer sample; PES: polyethersulfone.

We draw our fibers from a preform in the ambient environment which was fabricated by one-step multimaterial co-extrusion [34], details are in Appendix-1. The fiber preform consists of a $As_2Se_{1.5}S_{1.5}$ core, a $As_2S_3$ cladding, and a PES jacket with diameter ratios core : cladding : jacket = 2.5 : 8.75 : 12 mm. The core/cladding diameter ratio and the glass compositions used may be readily varied by changing the structure of the extrusion billet and the design of the die. The preform is drawn in two steps in order to reach to 10 μm core size. In each step, the preform is prepared by rolling a 125-μm-thick PES film around it to reach to the desired diameter.

The final fiber consists of a 10-μm-diameter core and a 35-μm-diameter cladding, embedded in a 1.2-mm-diameter PES jacket (Fig. 2). The thick built-in PES jacket is thermally compatible with the ChG used, so the fiber can be tapered without removing the polymer. The core and cladding materials are $As_2Se_{1.5}S_{1.5}$ and $As_2S_3$, respectively. The refractive index contrast between the core and cladding,

measured by an interferometric method (will be explained in more details in the dispersion characterization section), is about 0.27. The large index contrast can be useful for mode confinement and dispersion engineering.

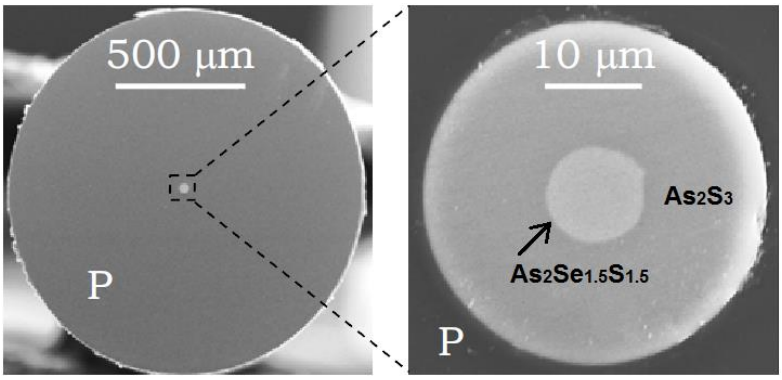


Fig. 2. Scanning electron microscope (SEM) images of the fiber (left) full cross section, and (right) ChG core/cladding region.

### 1.2. Mechanical Properties of the Fiber

One of the main drawbacks of ChG fibers is the poor mechanical properties. In Fig. 3-a, the result of tensile-strength test on a 400-µm-thick bare $As_2Se_3$ fiber is presented. The test was performed using a tensile-strength-test machine; in which the two ends of a 15-cm-long fiber were fixed in a pair of grippers, as one of the grippers slowly moved away from the other one (speed of 1 mm/min), the sample was gradually extended and the amount of applied axial force and extension in the sample-length was accurately measured by the machine. According to the measurements the fiber can only tolerate low axial stress and breaks at about 1-N axial force.

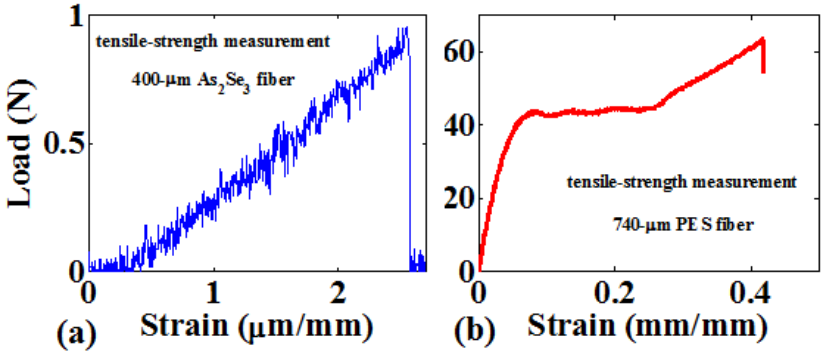


Fig. 3. Tensile-strength measurement for (a) a bare 400-µm-thick chalcogenide fiber and (b) 740-µm-thick PES fiber.

To enhance the mechanical durability of commercial ChG fibers against axial stress, a polymer jacket is coated on the fiber. Since the coated polymer is not thermally compatible with the glass, it burns when heated for fiber tapering.

The thick built-in PES jacket in our fiber structure is thermally compatible with the ChGs and doesn't need to be removed before tapering. Since the PES jacket is more than 99% of the fiber volume, the mechanical robustness of the fiber is derived from the polymer, while the optical functionality of the fiber depends on the glass core and cladding. A similar tensile-strength test has also been performed on a 740-µm-thick PES fiber (Fig. **3**-b). The durability of the PES fiber is about two orders of magnitude larger than that of ChG fiber.

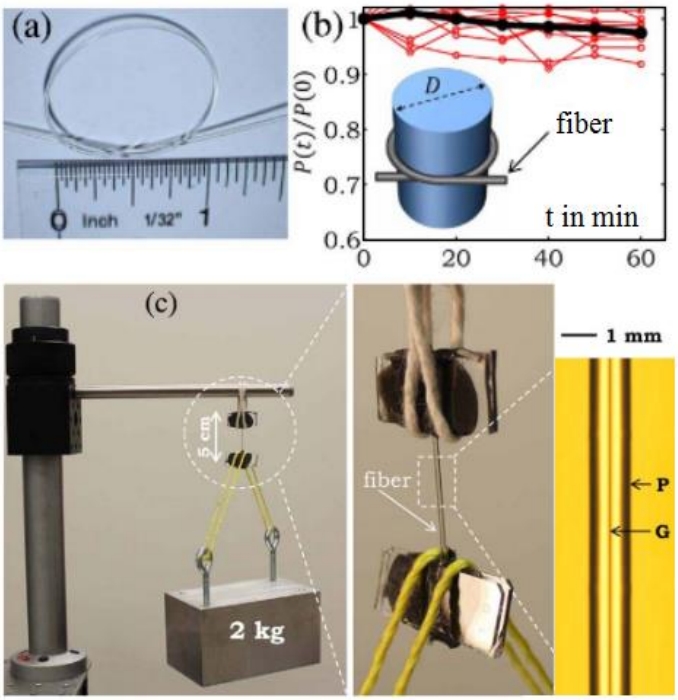


Fig. 4. (a) A 1-mm-diameter fiber tied in a 1-in.-diameter knot. (b) Transmission over time for 10 fibers after bending the fiber with 0.5-inch-bend diameter. The black curve is the average of all the measurements. (c) A 2 kg weight hanging from a 5-cm-long fiber. The inset shows the hanging mechanism. The fiber is attached to microscope slides using epoxy while keeping the ends free for optical measurements. (d) A robust multimaterial taper. The inset is a micrograph of the taper center.

The robustness of these composite ChG fibers is illustrated in Fig. 4. We measured the transmission over time (at 1.55µm) after bending a GP fiber for 10 min intervals. There was no

change for 1 inch bend diameter and larger, and we find no plastic memory in knots with diameters larger than 1 inch [Fig. 4-a]. Results for a 0.5 inch bend diameter are plotted in Fig. 4-b. The transmission did not decrease after an hour by more than 10% (5% on average).

We also investigated the effect of axial stress on optical transmission. We hang a 2 kg weight from multiple 5-cm-long fiber sections [Fig. 4-c] for 18 hours each and then measure the transmission (at 1.55 μm): it was unaffected in this experiment (compare to [49]). The fiber thus withstands 14.6 Kpsi (≈25.5 MPa) with no change in its performance over this extended period of time. This sets a lower limit on the fiber strength. Although the ChG diameter here is only 10 μm, the polymer jacket nevertheless allows for convenient handling and reduced ageing of the fibers. Therefore, the optical properties of the fiber are determined by the ChG, while the mechanical properties are determined by the polymer. Separating the functionalities in this way allows for them to be optimized independently.

### 1.3. Fiber Tapering

We produced fiber nano-tapers without removing the polymer using a home-built tapering system. The fiber is inserted in a heating zone for a fixed time interval before both fiber ends are pulled symmetrically in opposite directions (Fig. 5). There are three controllable tapering parameters: (1) temperature T, which determines the viscosity; (2) tapering distance, which determines the reduction in size; and (3) tapering speed, which determines the tapering time [36]. These three parameters allow us to exercise considerable control over the taper axial profile and results in robust nanotapers.

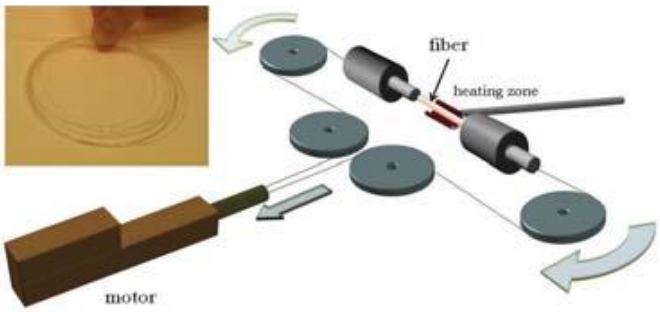


Fig. 5. Tapering setup. Inset shows the fiber used in the tapering experiments.

Although glass-fiber tapering has been studied extensively [37], our ChG-polymer hybrid fiber reveals different tapering dynamics since the polymer, which is the principle material component in the fiber, dictates its mechanical properties. Upon heating, the stress stored in the fiber polymer cladding during drawing and associated axial elongation (resulting in molecular alignment in the polymer) is released in the heated section. During fiber drawing, tension is determined in grams (equivalent force) by a force-meter that measures the restoring force from the fiber being pulled. The tension is determined by the drawing temperature, the drawing speed, and the downfeed speed of the preform into the draw-tower furnace.

Consequently, the polymer undergoes plastic deformation and shrinks away from the heating zone to accumulate at its edges (Fig. 6). At the center of each sample, the fiber diameter is reduced the most (the minimum core diameter at the midpoint is referred to hereafter as $d_c^{min}$), producing a tapered shape along the axis. Sectioning the fiber at different positions along the taper axis and examining the cross sections reveals that the core diameter scales approximately at a constant ratio with the outer diameter. As a result, we will take the axial variation of the fiber outer diameter along the nano-tapers to be an indication of their core diameters.

We find that the size and shape of the swelling or bulges thus formed depend on both the tapering parameters and the fiber-drawing tension. To study the effect of tapering temperature on the polymer swelling, we prepared five identical fiber samples drawn under 40-g equivalent tension and mounted them with fixed ends in a 20-mm-long heating zone (5-mm-long uniform heating section) and heated

them for 40 s at different temperatures without pulling the sample ends (Fig. 6). It is clear that as the tapering temperature increases, the deformation in turn increases.

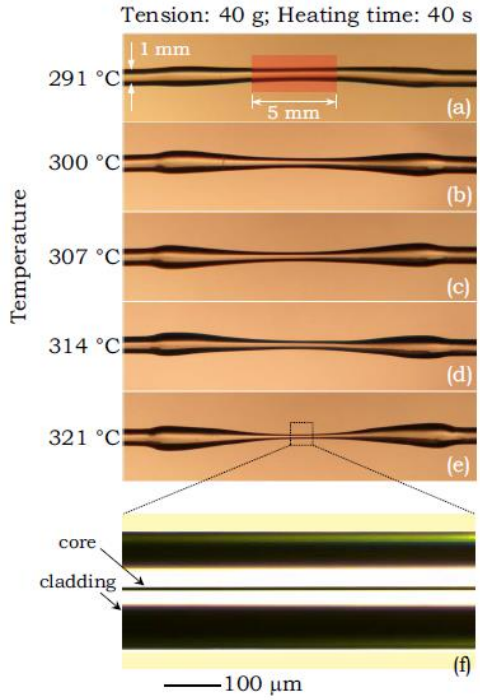


Fig. 6. Fiber axial plastic deformation upon heating in a tapering setup with 5-mm-wide uniform heating zone – corresponding to the red rectangle in panel (a). Panels (a) through (e) are transmission optical micrographs that correspond to identical samples (equivalent drawing tension of 40 g) at different temperatures for 40 s. Initial fiber outer diameter is 1 mm. (f) Transmission optical micrograph showing a magnified side image of the intact G1 core inside the PES cladding. The black symmetric outer portions of the cladding in the microscope image result from the curvature of the taper outer surface.

In another experiment, samples from three fibers – that were drawn under different tension – were heated at fixed temperature, and fiber deformation was observed in real time (Fig. 7). Our observations confirm that plastic deformation is more pronounced for a fiber drawn under higher tension. To reduce the effect of plastic deformation during tapering, we subsequently draw the fibers at low tension.

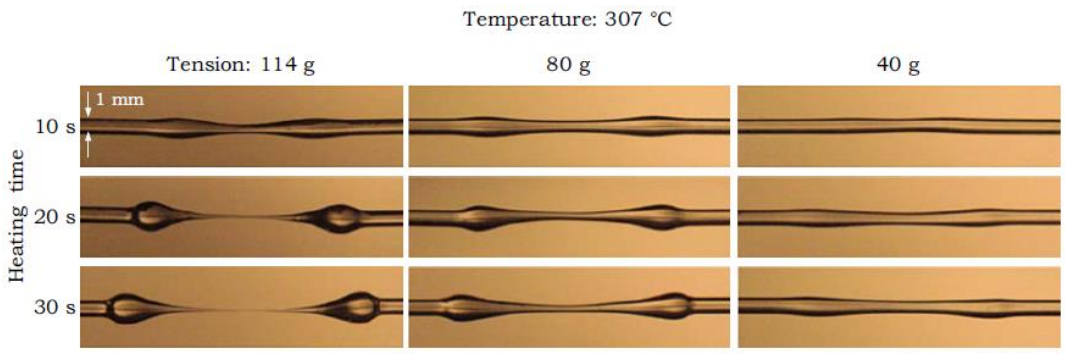


Fig. 7. Dependence of the axial plastic deformation upon heating in a tapering setup (see Fig. 6) on the tension during fiber drawing and tapering time. Each panel is an optical transmission micrograph of a fiber sample with initial fiber outer diameter 1 mm. The tapering temperature is held fixed throughout and the fiber-drawing tension is constant in each column.

Now, by also applying axial pulling force during tapering, we may control the length of the produced taper while maintaining minimal deformation at the edges. The unique aspect of the polymer jacket is that it enables tapering the samples, thereby reaching sub-micron-diameter cores while remaining robust enough for convenient handling. For example, the taper shown in Fig. **8**-a with 400-nm core diameter has a ≈ 50 μm outer diameter. Moreover, in Ref. [38] we demonstrate stable tapering of a polymer-embedded ChG nanowire to sub-5-nm-diameter. In our optical characterization experiments, we typically cut the tapered section of the fiber, fix it on a glass slide using epoxy, and then polish the facets [Fig. 8-b]. A section through the mid-point of such a taper [Fig. 8-c, Fig. **8**-d] reveals that the fiber structure is maintained.

Finally, we note that care must be taken during tapering to avoid the onset of fluid instabilities, such as the Plateau-Rayleigh capillary instability, that may be induced during tapering when the ChGs are in a low viscosity state. Such a fluid instability may result in the breakup of the continuous ChG core into isolated spheres held stationary in the polymer cladding [36,39].We have already reported [36] the restrictions on tapering speed and temperature that enable us to avoid such phenomena and obtain axially continuous nano-tapers.

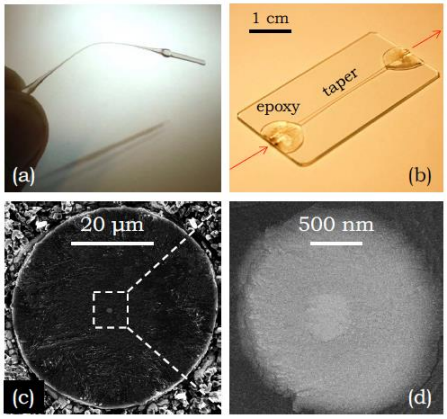


Fig. 8. (a) A robust nano-taper with minimum core midway along the sample dcmin = 400 nm. (b) A nano-taper mounted on a glass slide and is fixed using epoxy, after which the facets are polished. (c) SEM micrograph of the nano-taper cross section at the taper mid-point (corresponding to minimum diameter). (d) Higher-magnification SEM micrograph highlighting the ChG core/cladding structure; compare to Fig. 2-b.

Playing with the three controllable parameters we have been able to make tapers with $d_c^{min}$ down to 10s of nanometers and lengths up to 10s of centimeters. Because the fiber core, cladding and jacket are all tapered with the same ratios (confirmed experimentally by taking SEM micrographs of the tapers cross-section), the size of fiber core diameter is estimated by measuring the outer diameter of the fiber. An axial profile of a typical nanotaper (core diameter along the taper length) with $d_c^{min}$ = 250 nm is shown in Fig. 9-a. The fiber core diameter is approximately uniform along 70% of the taper length and the transition sections at the two ends are not longer than 30% of the whole length. This is important since the hampered of ultra-short pulses is hampered in ChG fibers with due to their large normal dispersion; however the large anomalous dispersion in the nanotapers can compensate for that.

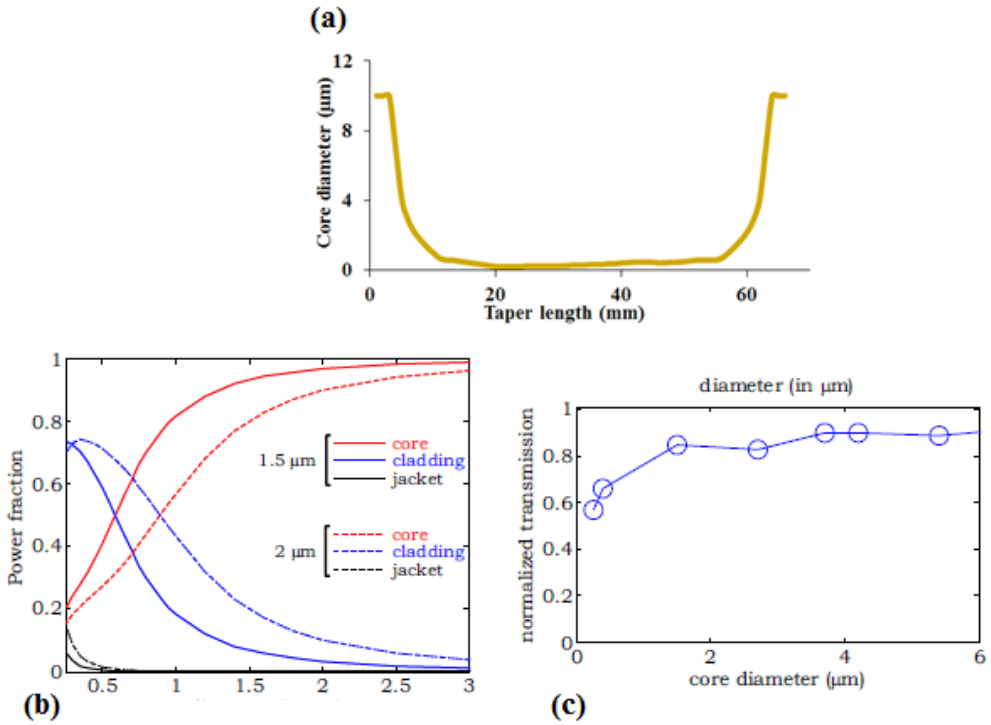


Fig. 9. (a) Axial profile of the core of a nanotaper with $d_c^{min}$ = 250 nm. (b) Power distribution of fundamental mode in the core, cladding and jacket of the fiber as a function of core diameter, calculated for 1.55 and 2 μm wavelengths. (c) Transmission loss of several tapers with different dcmin, measured at λ=1.55 μm in 25-mm-long tapers – normalized to the transmission in an equal length of non-tapered fiber.

To study the power distribution of the fundamental guided mode in fiber core, cladding and polymer jacket, we performed a set of systematic calculations at two wavelengths of 1.55 and 2 μm (Fig. 9-b). For large core sizes (> 2 μm), about 99% of the optical power at 1.55 μm is confined in the fiber core. As the core size decreases some part of the power starts entering the cladding. For core diameters smaller than 500 nm, the optical power enters the jacket. Around 7% of the light propagates in the jacket of a fiber with 250-nm-thick core. For longer wavelengths the mode confinement in the fiber core is expected to be less; for instance, 15% of the energy of the fundamental mode at 2-μm-wavelength enters the fiber jacket. This is not desired for MIR applications due to large material loss of the PES polymer at long wavelengths (Fig. 1-c). Hence based on the application an optimum core diameter has to be defined.

Measurements of the optical transmission of 1.55-μm CW laser light in several 25-mm-long tapers and different core diameters is shown in Fig. 9-c. When the core diameter is reduced below 1.5 μm, the transmission is significantly reduced. One potential reason is that local scattering centers in the glass matrix play a more significant role here than they usually play in the larger diameter fibers before tapering.

# CHAPTER 2
# DISPERSION CHARACTERIZATION

## 2.1. Chromatic Dispersion of Chalcogenide Glasses

As mentioned before, ChGs are endowed with several salutary features that make them excellent candidates for applications in MIR nonlinear fiber optics. This potential is thwarted, however, by the large normal group velocity dispersion (GVD) in the infrared [50], which distorts ultrashort optical pulses [51] and reduces the effective optical nonlinearity [48]. Furthermore, in some applications, such as supercontinuum generation, the GVD sign and magnitude play a crucial role, and hence must be precisely controlled [21, 52]. To harness the useful features of ChGs in MIR nonlinear fiber optics, the dispersion issue must be addressed.

Several approaches have been pursued to obviate the high bulk-ChG GVD through engineering the waveguide dispersion. In one approach, ChG photonic crystal fibers (PCFs) [18, 22] have been developed for GVD control [53]. The difficulty of ChG processing, in addition to the low viscosity of typical ChGs compared to that of silica glass [54, 55], have made progress along these lines slow since it is difficult to precisely and uniformly control the nanoscale trusses and wires required in the PCF cladding. An alternative approach relies on fiber tapering to modify GVD through dimensional control [20, 56] or hanging-core ChG fibers [18, 23]. Tapering also enhances the nonlinearity by increasing field confinement in high index-contrast structures [57], but is hampered by the unfavorable mechanical properties of ChGs [49].

We have recently reported a new approach for fabricating composite ChG-polymer preforms from which robust ChG fibers are drawn: one-step multimaterial preform co-extrusion [34]. This process produces ChG preforms provided with a thick built-in thermoplastic polymer jacket that is thermally compatible with the ChG. This feature has important consequences for the prospects of ChG fibers. First, the built-in polymer jacket improves the mechanical strength of the fiber with

respect to both bending and extensional forces [34]. Second, since the ChG and polymer are thermally compatible, the drawn fiber may be tapered without removing the polymer jacket [19, 36, 38]. Third, the process facilitates the fabrication of fibers with large core/cladding index contrasts (ncore−nclad nclad ≈ 0.15 in Ref. [34]). This procedure thus yields a new generation of ChG fibers that alleviates the traditional concerns of their mechanical strength and simultaneously opens up routes to new designs for GVD control and nonlinearity enhancement.

In this chapter we present the results of systematic measurements of the GVD parameter $\beta_2$ [48] at wavelength $\lambda$=1.5 μm in bulk ChGs, in high-index-contrast composite ChG fibers produced by the above-described process, and in robust ChG nano-tapers. We measure $\beta_2$ using spectral interferometry [47] after each fabrication step in order to detect potential effects attributed to the specific thermal processing associated with this new fiber production methodology. We isolate the contribution of waveguide dispersion and find excellent agreement with calculated values across both normal and anomalous waveguide dispersion regimes. Furthermore, we measure GVD in bulk ChGs at $\lambda$= 2 μm to assess the utility of thulium fiber lasers that are emerging as a potential pump source for MIR nonlinear fiber optics [58–62]. By combining the bulk $\beta_2$ measurements at $\lambda$=2 μm with calculated waveguide GVD, we present designs for all-solid zero-GVD ChG fibers.

This study is further motivated by the scarcity of reported direct GVD measurements in ChGs. Typically, ChG GVD is estimated from the measured wavelength dependent refractive index ($As_2Se_3$ in Ref. [63]) and $As_2S_3$ in Ref. [64], carried out recently using ellipsometry [65] and the prism-coupling technique [66]. The only reports on direct measurement of $\beta_2$ in ChGs are for bulk $As_2S_3$ at 1.3 μm [67]; $As_2Se_3$ fiber [68]; $As_2Se_3$, $Ge_{15}Sb_{20}S_{65}$ [69], and $As_2S_3$ [70] microstructured fibers at 1.5 μm. Moreover, since short, few-centimeter-long tapers are expected to be particularly important in MIR supercontinuum generation [20], it is crucial to accurately assess the effect of tapering on ChG fiber GVD. To the best of our knowledge, there have been no reported GVD measurements in ChG tapers. The results presented here on direct $\beta_2$ measurements in bulk samples, fibers, and nano-tapers

help close that gap. We present the results of nonlinear characterization of these fibers and nano-tapers elsewhere [19, 71].

## 2.2. Measurement Setup and Procedure

Fiber dispersion measurement techniques may be classified as pulse-delay (or time-of-flight), phase-shift, or interferometric methods. The pulse-delay technique is suitable for large group delays by determining the differential delay between optical pulses of different wavelengths [66, 67]. This method is typically used for long fibers, but recent efforts have extended it to shorter lengths [68, 69]. In the phase-shift method, sinusoidally modulated broadband light is coupled to the fiber and the delay between two selected wavelengths is extracted from their relative phase shift, subject to phase-wrapping ambiguities [70]. Interferometry resolves group delays down to 0.1 fs and is thus suitable for short fiber samples [71, 72]. We measured $\beta_2$ here using spectral interferometry [73] in a single-mode-fiber-based Mach-Zehnder interferometer (MZI) with the sample placed in one arm (sample arm) and a fixed delay in the other (reference arm); see Fig. 10. The same procedure was used for measurements at $\lambda = 1.5$ and 2 μm, except for the use of a different light source and detector. Light input to a fiber coupler is split between the reference and sample arms of the MZI. In the reference arm we place a free-space optical delay $\tau$ and a variable attenuator. In the sample arm, light is coupled out of the SMF, is collimated, traverses the sample, and is then coupled back into a SMF fiber (Fig. 10). Three spectra were recorded for each sample by means of an optical spectrum analyzer (OSA): the sample spectrum $I_s(\lambda)$ obtained by blocking the reference MZI arm; the reference spectrum $I_r(\lambda)$ obtained by blocking the sample arm; and the output spectrum $I_o(\lambda)$ obtained by superposing the sample and reference spectra.

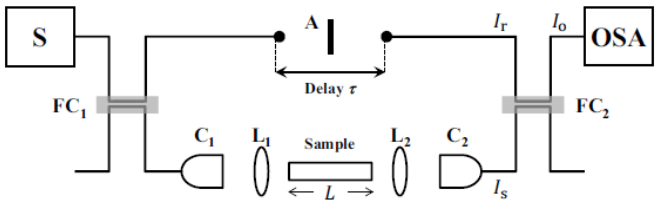


Fig. 10. Setup for measuring $\beta_2$. S: source, FC: fiber coupler, C: collimator, L: lens, A: attenuator (to increase fringe visibility), and OSA: optical spectrum analyzer. Solid lines are single-mode fibers.

The interference term was extracted from $I_o$, $I_s$, and $I_r$:

$$\mathbf{cos}(\boldsymbol{\Delta\phi}) = (\mathbf{I}_o - \mathbf{I}_s - \mathbf{I}_r)/(2\sqrt{\mathbf{I}_s\mathbf{I}_r});\ \mathbf{where}\ \boldsymbol{\Delta\phi} = \boldsymbol{\phi}_s - \boldsymbol{\omega\tau} + \boldsymbol{\phi}_B.$$

Here $\tau$ is the delay, $\omega$ is the optical frequency, $\boldsymbol{\phi}_B$ is a background phase estimated with the sample removed, and $\boldsymbol{\phi}_s$ is the sample phase. We extract $\boldsymbol{\Delta\phi}$ versus wavelength directly from $\mathbf{cos}(\boldsymbol{\Delta\phi})$ making use of the fact that the phase difference between each two successive peaks in $\mathbf{I}_o(\lambda)$ is $2\pi$. In order to accurately estimate the average wavelength difference between the peaks, amplitude modulation and noise were filtered from $\mathbf{I}_o(\lambda)$ in the Fourier domain [Fig. 11-a, Fig. 11-b]. This is particularly important when measurements are carried out at 2 μm in order to discriminate against the fine atmospheric absorption lines that overlay the measured spectra [Fig. 11-d, Fig. 11-e].We then estimate $\beta_2$ by fitting $\boldsymbol{\Delta\phi}$ to a second-order polynomial and averaging 10 measurements for each sample, and then repeating the experiment at 6–8 different positive and negative delays [Fig. 11-c, Fig. 11-f].

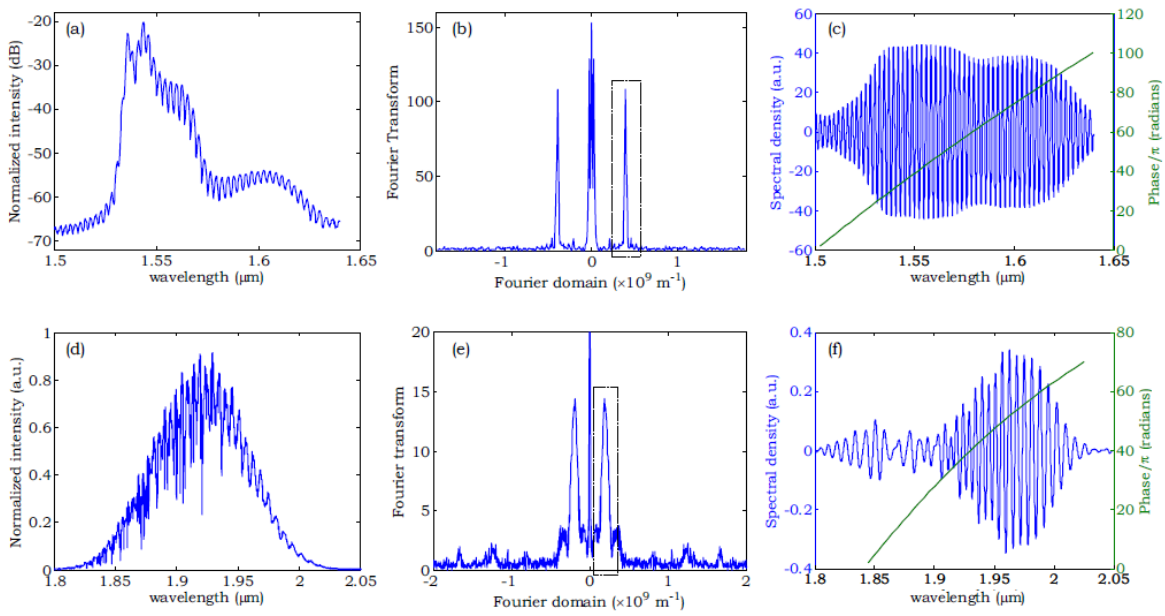


Fig. 11. (a) Spectral interference fringes in the output spectrum $I_o$ (λ) (note the logarithmic vertical scale) obtained using an OSA (Advantest Q8381A). The sample here is the BK7 bulk cube and the source is amplified spontaneous emission (ASE) from an EDFA (EAU-200-c, IPG Photonics). (b) The Fourier transform (FT) of $I_o$ (λ). The black dashed box corresponds to the portion filtered out to extract the interference fringes. (c) Filtered spectral power density obtained by taking the inverse FT of (b) and the extracted spectral phase Δϕ (λ). (d)-(f) are similar to (a)-(c) except that the source is ASE from a thulium fiber laser, the OSA is Yokogawa AQ6375 and the sample used is a bulk As2S3 disc; see Fig. 1-a, lower-left inset.

### 2.3. Dispersion of Bulk Samples and the Fiber

In the case of bulk samples in the form of 10-mmdiameter ChG discs, light is collimated in free space by C1, traverses the sample and is then coupled back into an SMF via a second collimator C2 (lenses L1 and L2 are removed in this case; see Fig. 7). We measured $\beta_2$ at λ=1.5 μm and 2 μm; see Fig. 9. As a reference, we measured $\beta_2$ for a 1-inch cube of BK7 glass and compare it with those of the bulk ChG samples (Table 1).We find that GVD is normal and decreases with wavelength in the ChGs, while GVD is anomalous and increases with wavelength in BK7. This may be understood by noting that λ=1.5 μm is above the zero-dispersion wavelength of BK7 but below that of ChGs. Note also the increase in GVD as Se replaces S in the ChG matrix. We used the same setup to also measure the refractive index of the samples. The fringe spacing in $I_o$ (λ) is longest when the optical path lengths are equal in both MZI arms. We adjust the optical delay in order to achieve this condition both in the presence and absence of the sample, from which we estimate the refractive index n (with ±0.015 precision).The measured indices at λ=1.5 and 2 μm are reported in Table 1. The measured

GVD values here for λ=1.5 and 2 μm are much larger than those associated with typical oxide glasses, which poses difficulties in using ultrafast pulses for nonlinear applications in ChG fibers. We shall use these measured values of n and $\beta_2$ below to guide the design of zero-GVD all-solid ChG fibers.

Table 1. Measured bulk index n and GVD β2 in ps2/km at 1.55 μm and 1.95 μm wavelengths. The indices n are estimated within ±0.015.

| Sample | Glass | $n$ 1.55 | $\beta_2$ 1.55 | $n$ 1.95 | $\beta_2$ 1.95 |
|---|---|---|---|---|---|
| Ref. | BK7 | 1.516 | -21 | — | -32 |
| G1 | $As_2Se_3$ | 2.904 | 978 | 2.876 | 762 |
| G2 | $As_2Se_{1.5}S_{1.5}$ | 2.743 | 670 | 2.645 | 554 |
| G3 | $As_2S_3$ | 2.472 | 474 | 2.456 | 383 |

## 2.4. Dispersion of Fiber Samples

The procedure used for bulk samples was also implemented for measuring the GVD in fiber samples, all of which have 10-μm-diameter cores. In this case, light collimated by $C_1$ is then focused via a lens $L_1$ into the fiber. $C_1$ was chosen to match the fiber fundamental mode. The output light is collimated with a lens $L_2$ (identical to $L_1$) before being coupled back into an SMF fiber via collimator $C_2$. Although the fiber samples are multi-mode, we ensure that the measured $\beta_2$ is that of the fundamental mode by monitoring the existence of interference fringes in the sample spectrum $I_s$ (λ) with the reference arm blocked, which reveals the potential excitation of multiple modes. The measured $\beta_2$ for 2.5-cm-long fiber samples (Table 2) differ only slightly from the bulk core glass. This is expected from the small values of waveguide GVD predicted theoretically at large core diameters and large core-cladding index contrast. We computed the waveguide GVD for the fundamental mode in COMSOL using the measured indices (Table 1) and structural dimensions for the fibers (Fig. 12-b). We then estimate the fiber GVD by combining the measured bulk GVD and calculated waveguide GVD, and find this estimate in good agreement with the measured fiber GVD for all three samples (see Table 2).

Table 2. Measured (Meas) and simulated (Sim) fiber GVD $\beta_2$ at 1.55 μm in $ps^2/km$; Jacket: polymer outer jacket. $G_1$, $G_2$ and $G_3$ are defined in table 1.

| Sample | Core | Clad. | Jacket | $\beta_2^{(Meas)}$ | $\beta_2^{(Sim)}$ |
|---|---|---|---|---|---|
| Fiber I | $G_1$ | $G_3$ | PEI | 968 | 967.2 |
| Fiber II | $G_2$ | $G_3$ | PES | 685 | 659.4 |
| Fiber III | $G_1$ | – | PES | 915 | 966.8 |

## 2.5. Dispersion of Nanotaper Samples

Finally we measured $\beta_2$ for the robust nanotapers prepared from Fiber II following the same procedure used for the fiber samples. The measured diameter profiles shown are given in Fig. 12-a, showing minimum core diameters $d_c^{min}$ at the nano-taper midpoints of 1.4 μm, 600 nm, 400 nm, and 330 nm (Table 3).

Table 3. Measured (Meas.) and simulated (Sim.) average GVD $\overline{\beta_2}$ at 1.55 μm in $ps^2/km$ for Fiber-II nano-tapers.

| Sample | $d_{min}$ | $L$ (cm) | $\overline{\beta_2}^{(Meas)}$ | $\overline{\beta_2}^{(Sim)}$ |
|---|---|---|---|---|
| Taper I | 1.4 $\mu$m | 2.1 | 640.8 | 621.4 |
| Taper II | 600 nm | 3.7 | 817.0 | 801.4 |
| Taper III | 600 nm | 4.25 | 752.3 | 731.6 |
| Taper IV | 400 nm | 2.5 | 631.8 | 692.8 |
| Taper V | 330 nm | 4.9 | 640.6 | 676.1 |

The high index-contrast in conjunction with the large change in core diameter (starting from 10 μm at the untapered end and extending down to $d_c^{min}$) leads to very wide changes in local waveguide GVD along the taper. We measured the total GVD phase shift produced by the taper and then divided it by the taper length L to obtain an average GVD parameter (Table 2).

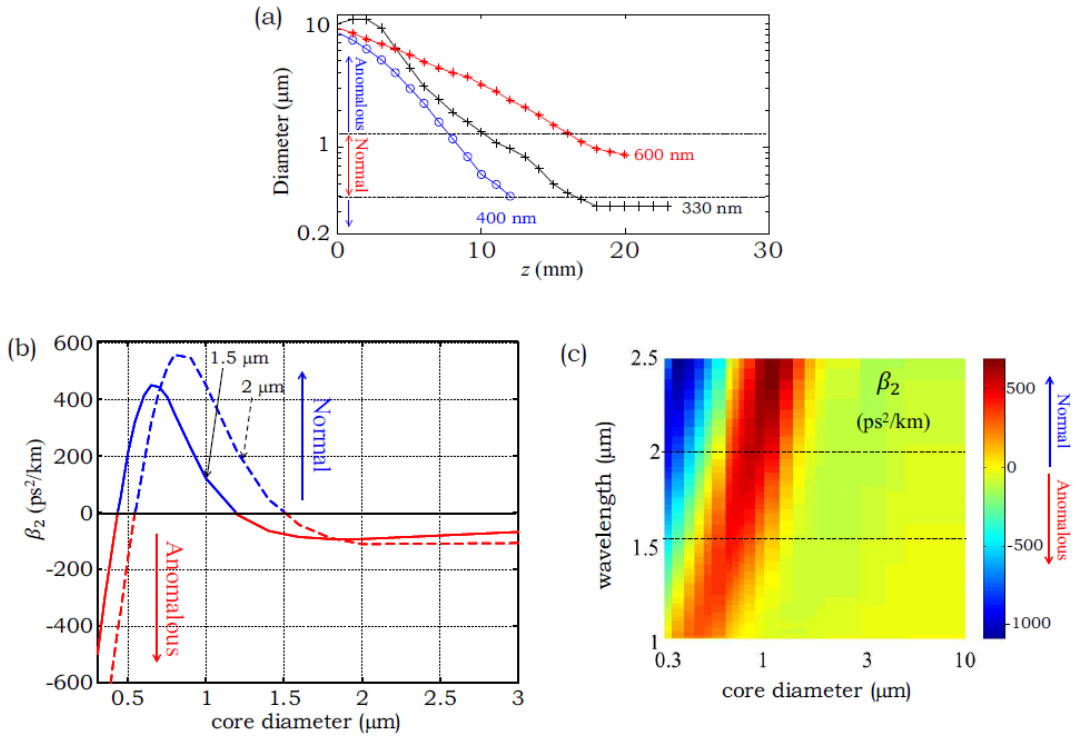


Fig. 12. (a) Measured diameter profile along the nano-tapers' axes (Table 3). Only half the length of the tapers is shown. The other half of each profile is a mirror reflection around the midpoint. Diameter ranges corresponding to normal and anomalous GVD are identified. (b) Calculated waveguide β2 for Fiber II at λ=1.55 μm and λ=1.95 μm for different core diameters. (c) Calculated waveguide β2 as a function of core diameter and wavelength. The two horizontal dashed lines correspond to the wavelengths used in our measurements.

We corroborate the measurements by computing $\overline{\boldsymbol{\beta_2}}^{(sim)} = \frac{1}{L}\sum_j \boldsymbol{\beta_2}(\boldsymbol{z_j})\,\boldsymbol{\Delta z} + \boldsymbol{\beta_2^{G_2}}$, where $\boldsymbol{\beta_2}(\boldsymbol{z_j})$ is the local fundamental-mode waveguide GVD at λ = 1.55 μm at positions $\boldsymbol{z_j}$ along the taper separated by $\boldsymbol{\Delta z}$ = 1 mm, and $\boldsymbol{\beta_2^{G_2}}$ is for the GVD of the bulk core glass $\boldsymbol{G_2}$. The waveguide GVD at 1.55 μm alternates with decreasing D from anomalous (1.2 μm<d) to nor mal (0.4<d<1.2μm) and then anomalous (d<400 nm). The second anomalous range is due to the interaction of the extended field tail of the fundamental mode in the ChG cladding with the polymer jacket. By combining the measured diameter profiles along the nano-taper axes (Fig. 12-a) with the calculated diameter-dependent $\beta_2$ (Fig. 12-b), we estimate $\boldsymbol{\beta_2}(\boldsymbol{z_j})$, from which we obtain the average $\boldsymbol{\beta_2}$. The measured and calculated $\boldsymbol{\beta_2}$ are in good agreement (Table 3). The results highlight the importance of the axial taper profile on engineering the nano-taper dispersion.

## 2.6. Designs for all-solid zero-GVD ChG fibers

The ability of our fabrication process [34] to produce a high-index-contrast core/cladding fiber structures opens the possibility of GVD control – necessary in most nonlinear wavelength conversion applications – using a simple all-solid structure. Using the measured indices and GVD parameters, we present examples of core-cladding structures that achieve zero-GVD in the infrared. First, consider the Fiber-II structure investigated above (table 2), but assuming an infinite $G_3$ cladding (no polymer jacket). A core diameter of d=4 μm achieves zero-GVD in the spectral range λ=3.1−3.2 μm (assuming a linear drop in bulk GVD with wavelength). In order to achieve zero-GVD at shorter wavelengths, a higher index-contrast is necessary. One approach is to use a tellurite glass cladding n=2.1 which produces zero-GVD at 2.2–2.3 μm (close to the thulium-fiber laser operating wavelength) with d=1.4 μm for either a $G_1$ or $G_2$ core. In other words, by controlling parameters that are accessible to our fabrication procedure ($n_{core}$, $n_{cladding}$, and d), we may shift the zero-dispersion wavelength to the nearinfrared where high-power laser sources are available.

# CHAPTER 3
# NONLINEAR CHARACTERIZATION OF NANOTAPERS

## 3.1. Nonlinearity in Chalcogenide Glasses

Despite the decades-long development of ChG fibers [11], harnessing their high optical nonlinearity has been curtailed by their poor power-handling capabilities [13, 14] and large normal group velocity dispersion (GVD) [15, 50]. To overcome these obstacles in ChG fibers, novel approaches are required, particularly to achieve broadband SCG. For example, cascaded Raman frequency shifting [10, 16, 17] has been used in conjunction with long pump pulses (tens of picoseconds to nanoseconds) to produce spectral broadening via stimulated Raman scattering. While the long pump pulses help reduce the deleterious impact of large GVD, the generated supercontinua are expected to be incoherent [74].

To date, three strategies have been explored to overcome the high ChG material GVD by balancing it with counteracting waveguide GVD. The first strategy relies on high-index-contrast composite fibers, such as ChG/silica step-index fibers [30], ChG/polymethyl methacrylate (PMMA) hybrid microwires [32, 75], and ChG-core/tellurite-cladding microstructured fibers [28]. The new material incorporated with the ChG in such heterostructures typically sets a limitation; for example, the high material loss of silica glass and PMMA at long wavelengths is a drawback in MIR applications. The second strategy makes use of dispersion-engineered photonic crystal fibers (PCFs) [12, 22, 29] and suspended-core fibers [18, 23, 24, 70], but these technologies have not yet reached the level of maturity of their silica-PCF counterparts. A third strategy utilizes bare ChG fiber tapers for dispersion engineering through an appropriate tapering ratio, while ensuring broadband single-mode guidance to produce SCG with a high-quality spatial profile [26, 76]. Indeed, As2Se3 tapers with a 1.2 μm waist diameter demonstrated an enhanced nonlinearity of 62000 times that of a standard silica single-mode fiber [26] (see also Refs. [27, 76–78]). While silica tapers have long been a source for SCG [25], bare ChG tapers are extremely difficult to handle due to the inferior

mechanical properties of ChGs compared to silica, which limits the utility of this approach despite its promise [ 76, 79, 80].

Our fiber fabrication approach explained in the first chapter resolves the traditional concerns of the mechanical fragility of ChGs without compromising their optical performance. In a hybrid fiber produced using this process; the optical properties are dictated by the ChG index-guiding structure, while the mechanical robustness derives from a millimeter-diameter built-in polymer jacket. In contrast to most alternative approaches, this process offers flexibility in choosing the geometric parameters (such as the core and cladding diameters) and gives access to a wide range of core and cladding ChG combinations and, thereby, provides control over their index contrast. Uniquely, the thermal compatibility between the ChG and the polymer allows for fiber tapering without first removing the polymer jacket, resulting in robust tapers that are easily handled and manipulated. Concomitantly, using ChGs jointly with a high core-to-cladding index contrast leads to strong confinement of the optical mode to the taper core [34], thereby enhancing the nonlinearity and enabling control over GVD. Furthermore, these nanotapers obviate the need for in situ tapering of ChG fibers [79, 80] and the complications associated with precarious handling of traditional bare ChG tapers. We have recently reported the first observations of octave-spanning infrared SCG in such robust all-solid nanotapers with strong field confinement [19] and have provided a detailed investigation of their linear properties and GVD characteristics [15].

In this chapter we present a systematic characterization of the nonlinear properties of robust, composite (multimaterial) ChG nanotapers produced using this novel fabrication methodology, which complements our study of their linear properties [15, 34]. Using the standard Zscan technique with femtosecond pulses, we measure the nonlinear index of refraction $n_2$ at a wavelength of $\lambda$=1.55 μm in the bulk glasses that are incorporated in our fibers and, thence, the nanotapers. We next estimate $n_2$ in the nanotapers via self-phase modulation (SPM) measurements at low peak powers in both the picosecond- and femtosecond-pulse regimes. The values of $n_2$ estimated in bulk ChGs and those

obtained in the nanotapers are in good agreement. These measurements provide the parameter values incorporated in a computational model we constructed for SCG in such nanotapers at higher peak powers. The predictions of this model are compared to SCG measurements using femtosecond pulses coupled to the nanotapers. The theoretical predictions and SCG measurements are in excellent agreement, thereby confirming the consistency and utility of our computational model. Our results clearly indicate the promise of robust composite ChG nanotapers produced using the multimaterial coextrusion approach as a viable technology to harness the unique capabilities of ChGs while circumventing some of their limitations.

### 3.2. Nonlinear Characterization of Bulk Chalcogenides

We start by characterizing the nonlinear characteristics of the ChGs of interest in bulk form. The ChGs used in fabricating the fibers and nanotapers investigated here were prepared from commercial glass (Amorphous Materials, Inc.) [34]. We produced 1-cm-diameter disk-shaped samples of three glasses: $As_2Se_{1.5}S_{1.5}$, $As_2Se_3$, and $As_2S_3$. 1.5-mm-thick samples were polished to sub-micrometer surface roughness.

The nonlinear refractive indices n2 of the ChGs were measured at $\lambda$=1.55 μm by the standard Z-scan technique [81] using ~100 fs (FWHM) pulses generated by an optical parametric generator/amplifier (OPA/OPG, TOPAS-C Light Conversion Ltd.); see Appendix-2 for details. The closed- and open-aperture Z-scan data (along with fitted curves) are shown in Fig. 13, for the $As_2Se_{1.5}S_{1.5}$ sample.

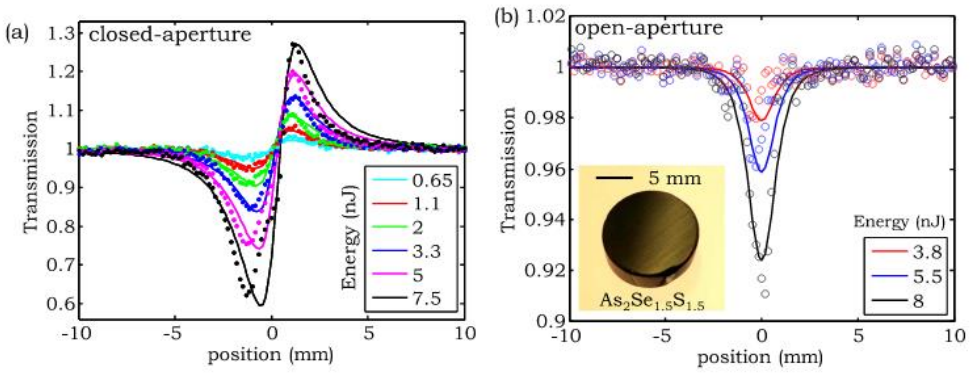


Fig. 13. (a) Closed-aperture and (b) open-aperture (three-photon absorption here) Z-scan results for a $As_2Se_{1.5}S_{1.5}$ sample at different incident femtosecond-pulse energies (see text and Appendix-2 for details). The dots are the measured values and the solid lines are the fitted curves. The inset in (b) is a photograph of the $As_2Se_{1.5}S_{1.5}$ sample.

After fitting the data, n2 was found for $As_2Se_3$ to be $(5.2\mp1.0)\times10^{-14}cm^2/W$, for $As_2Se_{1.5}S_{1.5}$ to be $(4.6\mp0.9)\times10^{-14}cm^2/W$, and for $As_2Se_3$ to be $(1.6\mp0.9)\times10^{-14}cm^2/W$. We note that the measurements for the $As_2Se_{1.5}S_{1.5}$ sample indicate three-photon absorption (3PA) in the open-aperture signal with a 3PA coefficient of $(5.5\mp2.5)\times10^{-2}cm^3/GW^2$ [Fig. 13-b]. This measurement is consistent with the result ≈8.7×10−2cm3⁄GW2 calculated from a two-parabolic-band model (a more complete analysis is provided in [82]) assuming the bandgap is ≈1.74 eV, which is based on the linear transmittance spectrum of this ChG composition [15]. For the other two samples, no nonlinear absorption was observed for the irradiances used and two-photon absorption is not expected at this wavelength.

## 3.3. Nonlinear Characterization of Robust Composite ChG nanotapers

### 3.3.1. Nanotaper Samples

We next investigate the nonlinear characteristics of robust composite ChG nanotapers produced using the novel fabrication approach described above. Our approaches to fiber preform fabrication, fiber drawing, and fiber tapering, in addition to linear optical and mechanical characterization of these unique fibers and nanotapers, have been reported elsewhere; see Refs. [15, 19, 34, 55]. The step-index fiber we investigate here consists of a 10-μm-diameter $As_2Se_{1.5}S_{1.5}$ core and a 35-μm diameter $As_2S_3$ cladding surrounded by a thick built-in 1.2-mm-diameter thermoplastic polymer jacket

(polyethersulfone, PES) that does not participate in the optical functionality of the fiber, but dictates its superior mechanical robustness compared to a conventional all-ChG fiber [34].

We plot the measured longitudinal profiles of the four nanotaper samples used in our measurements in Fig. 14-a. Other relevant parameters of the nanotaper Samples 1 through 4, such as the total length L, the minimum core diameter at the nanotaper axial midpoint $d_c^{min}$, and the optical transmission using CW laser light at λ=1.55 μm (raw transmission, which includes ≈ 21.6% Fresnel reflection at each facet) are listed in Table 4. Although the short transition regions in the samples between the tapered and nontapered sections increase the optical losses, they nevertheless reduce the energy transfer from the cladding modes back into the core modes at the end of the tapered sections [37].

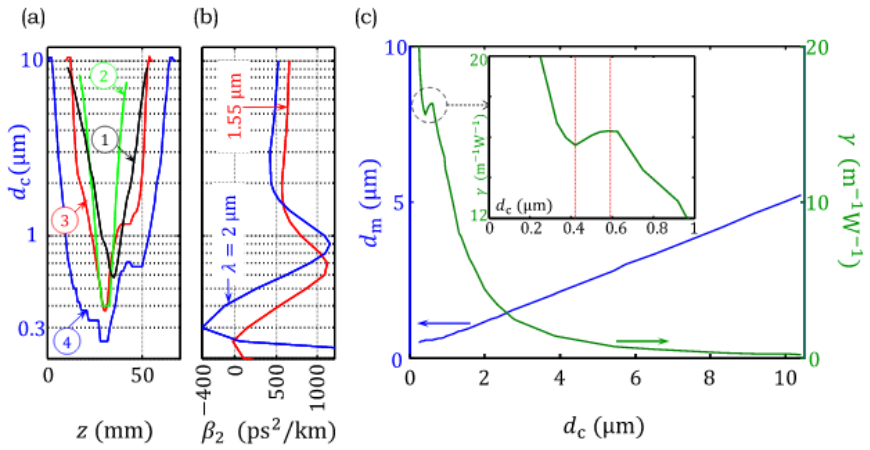


Fig. 14. (a) Longitudinal core diameter dc profiles of the four samples used in the experiments; z is taken along the nanotaper axis. ($d_c^{min}$, L)of Samples through 4 are: (580 nm, 42 mm), (400 nm, 25 mm), (375 nm, 46 mm), and (250 nm, 68 mm), respectively. See also Table 4. (b) The total GVD parameter $\beta_2$ as a function dc calculated at λ=1.55 and 2 μm. (c) The blue curve (left vertical axis) shows the diameter of the fundamental mode dm at λ=1.55 μm, which indicates the optical-mode confinement when compared to dc, and the green curve (right vertical axis) is the nonlinear coefficient γ of the fiber as a function of core diameter dc, calculated for the fundamental mode at λ=1.55 μm. The inset shows the region of the curve of γ that is encircled (dashed circle) and highlights the non-monotonic relationship between $d_m$ and $d_c$ at sub-micrometer core diameters (250 nm<$d_c$<1 μm). The two-dashed vertical lines in the inset correspond to dc=600 nm (where $d_m/d_c$ exceeds 1) and dc=450 nm (where confinement by the polymer jacket starts to dominate). See text for details.

To set the stage for our nonlinear optical characterization experiments, we plot two optical parameters that change with core diameter $d_c$, and thus vary axially along the nanotaper: total GVD at λ=1.55 μm and 2 μm [Fig. 14-b], and the nonlinear parameter $\gamma=2\pi n_2/\lambda A_{eff}$ [48] at λ=1.55 μm [Fig.

14-c]; here $A_{eff}$ is the effective core area (see Ref. [48]). The total GVD is the sum of the measured material GVD and the calculated waveguide GVD [15]. Note that the GVD changes rapidly with $d_c$ at the nanoscale due to strong field confinement effects (resulting from the large core/cladding index contrast) [15]. We plot $\beta_2$ also at $\lambda$=2 μm to highlight the change in $\beta_2$ with wavelength and also in light of the current availability of high-power Tm-doped fiber lasers [58–60, 62], which are potentially useful as pumps for SCG.

Table 4. Nanotaper Sample Parameters; Here dcmin is the minimum core diameter at the nanotaper axial midpoint; L is the nanotaper total length; T is the sample transmission (including the Fresnel reflection at the facets).

| Sample | 1 | 2 | 3 | 4 |
|---|---|---|---|---|
| $d_c^{min}$ (in nm) | 580 | 400 | 375 | 250 |
| $L$ (in mm) | 42 | 25 | 46 | 68 |
| $T$ (%) at $\lambda = 1.55$ μm | 35 | 32 | 28 | 26 |

The diameter of the fundamental mode dm (full width at $1/e^2$ from maximum) and the nonlinear coefficient $\gamma$ are plotted in Fig. 14-c as a function of $d_c$ at $\lambda$=1.55 μm. It is clear that three distinct regimes emerge in the dependence of $\gamma$ on $d_c$. For large $d_c$ (>3 μm), the fundamental mode is well confined to the core (>99%) due to the large core/cladding index contrast. In this regime, $d_m$ and dc are linearly related (with $d_m<d_c$). As dc decreases, a concomitant reduction in the mode diameter dm ensues, and consequently $\gamma$ increases. This linear trend changes with further reduction in dc, and at $d_c$~600 nm the ratio $d_m/d_c$ exceeds 1. At this point, the mode extends significantly out of the core and $\gamma$ therefore decreases with reduction in $d_c$ [Fig. 14-c, inset]. Finally, when $d_c$<450 nm, the mode extends further into the ChG cladding and reaches the polymer jacket. Due to the large index contrast between the cladding (n=2.472 for $As_2S_3$ at $\lambda$=1.55 μm) and polymer ($n_{PES}$=1.61 at $\lambda$=1.55 μm), the mode remains confined in the cladding and $\gamma$ increases again with further reduction in fiber diameter. Although $\gamma$ continues to increase by reducing $d_c$, the high infrared optical losses in the polymer [21] obviates the advantages accrued by further tapering. Hence, from these considerations we conclude that, for SCG applications using these hybrid nanotapers, the optimum $d_c^{min}$ value is several hundreds of nanometers, while L should not exceed a few centimeters to avoid heavy infrared losses in the

polymer jacket (which may be reduced by increasing the diameter of the ChG cladding). The nanotaper samples investigated here were prepared in accordance with these guidelines to confirm the design principles.

### 3.3.2. Nonlinear Characterization Methodology

We now proceed to describe the results of nonlinear characterization experiments carried out with these nano-tapers. Two classes of experiments were performed. In the first we obtained an independent measurement of $n_2$ from observations of spectral broadening resulting from self-phase modulation (SPM) using low peakpower laser pulses. In the second class of experiments we used higher peak-power pulses to observe SCG extending over one-octave of bandwidth. We employed a theoretical model that utilizes parameters extracted from our linear and nonlinear measurements to validate the spectral broadening observed. Both classes of experiments (SPM and SCG) were car carried out using the setup in Fig. 15. We used fiber-coupled lasers and the $\lambda = 1.55$ μm collimated beam was coupled in and then out of the 10-μm-diameter core of the nano-taper samples using a pair of 6.2-mm focal length aspheric lenses. An infrared camera (7290A Micron- Viewer) was used to monitor the beam profile and optimize the coupling into the core. The output spectrum was measured with 0.1-nm spectral resolution using an optical spectrum analyzer (OSA; Advantest Q8381A). Two laser sources at $\lambda = 1.5$ μm were used. The first is a femtosecond passively mode-locked fiber laser (Calmar, FPL-M2CFF) producing pulses with 400-fs FWHM pulsewidth at 20-MHz repetition rate and maximum peak power of 0.56 kW (corresponding to 4.5 mW average power). The second is a passively mode-locked Erbium doped fiber laser (PriTel, PFL-10000) producing picosecond pulses with 10-ps FWHM pulsewidth at 5 MHz repetition rate and maximum peak power of 80 W (corresponding to 4 mW average power).

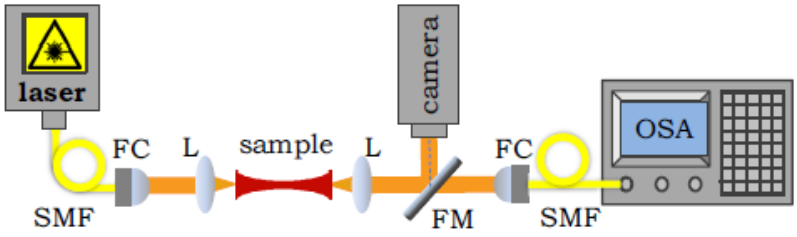


Fig. 15. Setup for nonlinear optical characterizations

### 3.3.3. Self-phase modulation (SPM) measurements

The goal of this experiment is to estimate $n_2$ of the ChGs in the nano-taper form-factor to confirm and complement the values obtained in bulk ChG. We extract $n_2$ from the total nonlinear phase shift [36] of an optical pulse traversing the nano-tapers, estimated from the spectral broadening. We made 4 samples for these experiments. (L, $d_c^{min}$) of the samples 1 through 4 are: (580 nm, 42 mm), (400 nm, 25 mm), (375 nm, 46 mm), and (250 nm, 68 mm), respectively. Coupling 1.7-mW input average power fsec pulses to nanotaper Sample-2 [Fig. 16-a] and 4.5-mW input average power psec pulses coupled to Sample-4 [Fig. 16-b] both led to the development of three distinct spectral peaks. Varying the input power using a variable attenuator leads to a gradually evolution of the output spectrum from the single-peaked input to the three-peaked spectra shown in Fig. 16. For comparison, the output optical spectrum was simulated by the split-step-Fourier method taking into account the axial variation in the optical mode, GVD, and $\gamma$. A main source of uncertainty in the initial simulation parameters stems from the need to estimate the power coupled into the fundamental mode at the nano-taper waist where most of the nonlinear phase accumulates. Several factors must be accounted for: input coupling efficiency, Fresnel reflection at the facets, linear fiber (material) loss, tapering loss, scattering, and potentially nonlinear absorption. The measured input and output power – for each power level and after accounting for Fresnel reflection – place upper and lower bounds on the power at the nano-taper waist. For each power level, we carried out the simulations by scanning both the uncertainty range of power between these two bounds and values for to $n_2$ to optimize the matching between the measured and simulated spectra. The $n_2$ values obtained from both the picosecond and femtosecond SPM measurements are $(3.75\pm1.45)\times10^{-14}$ $cm^2/W$ and (3.15e±0.85)×10−14 cm2/W,

respectively, in agreement with the values $n_2$ in bulk ChGs given above and measured through Zscan. The values are slightly lower than the $n_2$ value obtained in bulk $As_2Se_{1.5}S_{1.5}$ given above that was measured via the Zscan technique. This result is expected since the $n_2$ values obtained from the nanotapers combine the impact of both the core and the cladding ChGs (the cladding has lower $n_2$ than the core). The simulated spectra thus obtained are in good agreement with the experimental results [Fig. 16-c, Fig. **16**-d)].

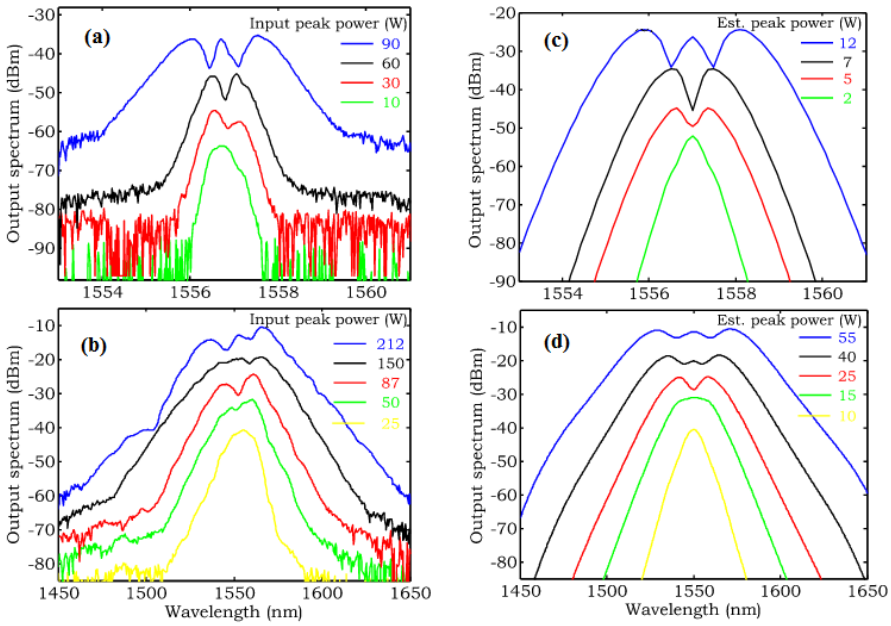


Fig. 16. SPM characterization results obtained in two different experiments: (a) picosecond pulses launched into nanotaper Sample 4 and (b) femtosecond pulses launched into nanotaper Sample 2. The power levels are the input peak powers for each sample without corrections for Fresnel reflection from the sample facets. (c) SPM simulation results for the two different experiments shown in (a) and (b): (c) picosecond pulses launched into Sample 4 and (d) femtosecond pulses launched into Sample 2. The power levels are the estimated peak powers in the tapered section of each sample after correcting for Fresnel reflections at the sample facets and nanotaper losses (see text for details).

### 3.4. Supercontinuum Generation (SCG) Measurements

The demonstration of visible and near-infrared SCG in silica PCFs [86] and tapers [25], more than a decade ago, has led to a flurry of fundamental studies in nonlinear fiber optics with applications in spectroscopy, frequency comb generation, and optical coherence tomography [52]. Recent efforts have aimed at extending SCG into the MIR where molecular fingerprints may be accessed. High MIR losses in silica have prompted the exploration of tellurite, ZBLAN, and ChG

fibers. For example, MIR SCG below 5 μm was produced using an 8 mm long tellurite PCF pumped with $\tau_p$=110 fs pulses of peak power $P_p$=17 kW at wavelength $\lambda_p$=1.55 μm [7], and an 8.5 m long ZBLAN fiber (nanosecond pulses, $P_p$=16 kW, $\lambda_p$=2 μm) [8]. The high losses beyond 4 μm in ZBLAN and tellurite glasses prevent extending the SCG further into the MIR except through the use of short fiber lengths and high $P_p$: the SCG from a 1-cm-long ZBLAN fiber ($\tau_p$=180 fs, $P_p$=50 MW, $\lambda_p$=1.45 μm) extended to 6.3 μm [87]. To produce SCG beyond 4–5 μm ChGs are the most prominent option due to their MIR transparency and high optical nonlinearity [2]. Previous studies of SCG in ChG fibers relied on femtosecond pulses, and special measures were implemented to combat the deleterious effects of the high normal group velocity dispersion (GVD) of ChGs. A 1–2.6 μm SCG was produced with $\lambda_p$=1.55 μm using a 30 cm long $As_2S_3$ PCF ($\tau_p$=400 fs, $P_p$=5.6 kW) [29] and a 1.3 μm diameter, 5 cm long tapered section of a 50 cm long $As_2S_3$ fiber ($\tau_p$=250 fs, $P_p$=0.8 kW) [20]. Longer wavelengths are generated using a longer wavelength pump: a 1 m ChG PCF produced 2.1–3.2 μm SCG ($\tau_p$=100 fs, $P_p$=1 kW, $\lambda_p$=2.5 μm) [88].

### 3.4.1. Pumping at 1.55-μm-Wavelength

#### 3.4.1.1. Picosecond Pulses

In this section we demonstrate infrared SCG, extending from 850 nm to 2.35 μm using picosecond pulses. The pump is a $\lambda_p$=1.55 μm mode-locked picosecond laser (Raydiance 010-503) with $\tau_p$=1 ps [autocorrelation trace in Fig. 17-b], FWHM bandwidth of 7.5 nm [Fig. 17-c], and repetition rate of 0.5 MHz. The beam spatial profile is shown in Fig. 17-d. The beam is coupled in and out of the taper using identical aspheric lenses $L_1$ and $L_2$ with 0.4 NA and 6.2 mm focal length [Fig. 17-a]. A near-field image of the beam exiting the fiber is monitored to ensure that light is confined in the core. The output beam is coupled into a 1-m-long single-mode fiber (SMF) via a fiber collimator, and delivered to an optical spectrum analyzer (OSA).

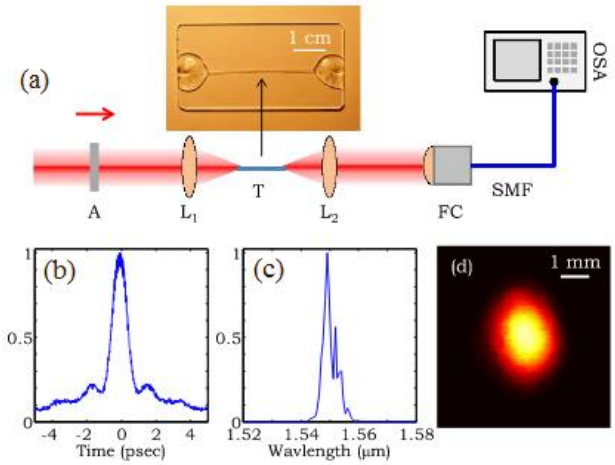


Fig. 17. (a) Schematic of the optical setup: A, attenuator; $L_1$, $L_2$, lenses; T, nanotaper; FC, fiber collimator; SMF, single-mode fiber; OSA, optical spectrum analyzer. (b) Autocorrelation trace, (c) spectrum, and (d) pump mode distribution 2 m from the laser. Since the beam lacks symmetry, the coupling efficiency was reduced compared to a symmetric spatial mode.

The output spectrum was recorded using two OSAs: up to 1.7 μm using Advantest Q8381A OSA, and 1.7–2.4 μm using Yokogawa AQ6375 OSA. The measured output spectra are plotted in Fig. 18 with increasing input $P_p$. At $P_p$=3.5 kW the output spectrum extends over more than one octave, from 850 nm to 2.35 μm. Except for the remaining pump, an octave is confined within 25 dB from the SCG peak. Note that this spectrum is in a single spatial mode delivered through the SMF. Furthermore, the GVD is normal along the taper and the SCG is thus expected to be coherent.

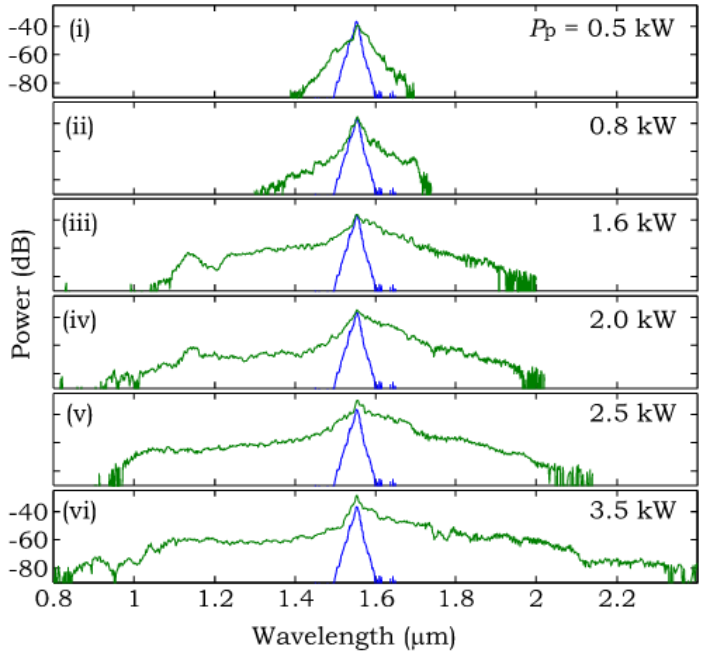


Fig. 18. SCG in robust ChG tapers. The measured output spectrum is plotted with increasing input pump power from (i) through (vi).

To simulate the nonlinear propagation dynamics of the pulse along the taper, we use the generalized nonlinear Schrödinger equation (GNLSE) [21] including terms that account for wavelength-dependent linear loss [89], GVD, self-phase modulation, Raman response, and self-steepening. Some of these parameters depend on $d_c$, so we first measure the taper profile and estimate $d_c$ along the axis. GVD is normal along the taper. The nonlinear parameter $\gamma$ depends on $d_c$, the field confinement, and the nonlinear indices $n_2$ for the core and cladding. At the input $\gamma$=0.23 $W^{-1}m^{-1}$ increases to a maximum value of 16 $W^{-1}m^{-1}$ at dc 770 nm, and reaches 15.7 $W^{-1}m^{-1}$ at midpoint. The Raman response function and Raman strength coefficient for $As_2Se_{1.5}S_{1.5}$ are taken to be an average of those for $As_2Se_3$ [90] and $As_2S_3$ [91]. Finally, the self-steepening is modeled to first order using an optical-shock time constant $\tau_s=1/\omega_p$ [21], where $\omega_p$ is the pump central frequency. We integrate the GNLSE using the symmetrized split-step method [20] after launching a linearly polarized transform-limited Gaussian pulse with a 1-ps intensity FWHM ($2^{15}$ points, 2 fs sampling period) in the fundamental mode. To ensure convergence, we adaptively change the axial step size to restrict the nonlinear SPM phase shift to 0.001 rad per step. For $P_p$=10 W (3kW) at the input, the axial step starts

at 10 μm (0.652 μm) and reaches a minimum value of 2.24 μm (17.2 nm). The simulation results are plotted in Fig. 19-a over the spectral and dynamic ranges used in Fig. 18 and show excellent agreement with the measured spectral broadening.

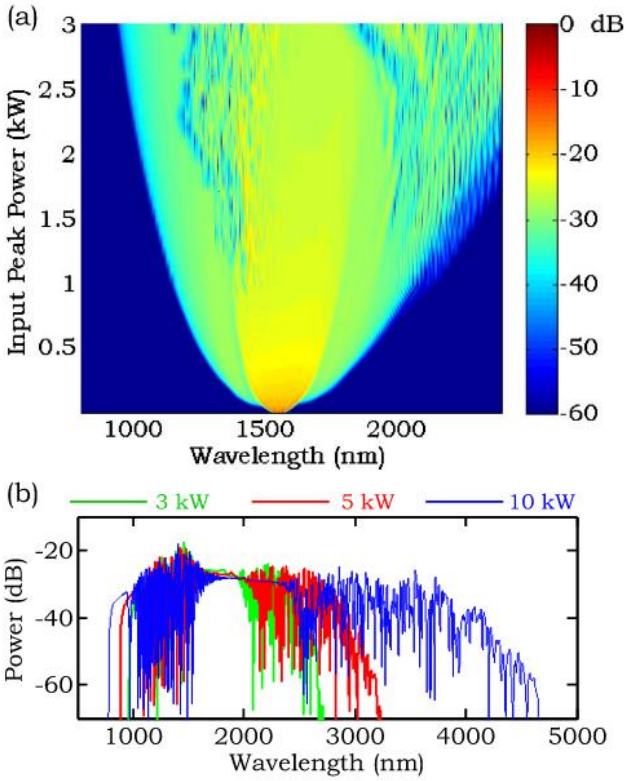


Fig. 19. Calculated spectrum at the nanotaper output with increasing input pump power obtained by integrating the GNLSE. See text for details. (b) Output spectrum for input $P_p$=3, 5, and 10 kW.

At higher input Pp, damage occurs at the input facet in the form of a depressed crater, but no damage was detected at the taper center. By repolishing the facet, the taper may be reused and the full spectrum generated. Since the intensity at the taper center is ≈ × 100 higher with respect to the input, this suggests that the damage is not due to the power-handling capability of the ChG, but instead the field discontinuity at the air/ChG interface. We thus expect that an antireflection coating at the fiber tip will enable coupling higher power. In Fig. 19-b we plot the calculated spectrum for $P_p$=10 kW showing the potential of the SCG to extend to 4.5 μm.

### 3.4.1.2. Femtosecond Pulses

Experiments were performed to demonstrate the potential of such robust multimaterial nano-tapers for efficient SCG. At relatively low power levels (peak-power ~100 W), we achieve hundreds of nanometers of spectral broadening in these nano-tapers. Moreover, the agreement between the measured supercontinua and their simulated counterparts that were obtained using the measured sample parameters further confirm the validity and consistency of our theoretical model. The fsec laser was coupled to three samples: (L, $d_c^{min}$) of the samples 1 through 3 are: (580 nm, 42 mm), (375 nm, 46 mm), and (250 nm, 68 mm). The supercontinuum produced by Sample-1 spans 1.3–1.75 μm, while that produced by Sample-2 was slightly broader to cover 1.2–1.9 μm attributed mainly to its lower GVD compared to Sample-1. The broadest spectrum was achieved by Sample-3, since it has the longest tapered section and the smallest $d_{min}$, resulting in one octave of bandwidth 1–2 μm [Fig. 20-a].

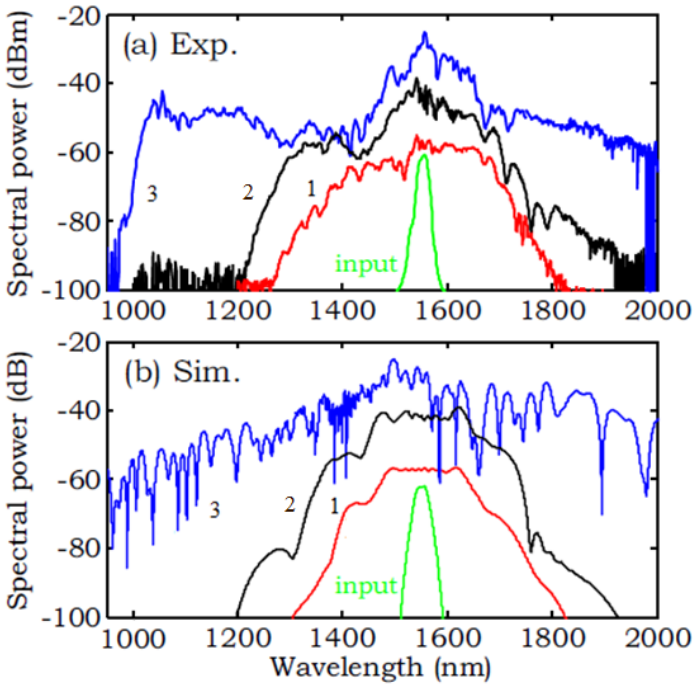


Fig. 20. (a) Measured and (b) stimulated continuums for samples 1, 2, and 3. The input pulse parameters are 3.5 mW input, 20 MHz, 400 fs. The power levels in the stimulated spectra are estimated for sample 1, 2 and 3 are 1 mW, 0.8 mW, and 0.85 mW, respectively.

Some slow power variations and drift (on the order of a few minutes) were observed in the spectra during the measurements. We suggest that these fluctuations originate from both thermal effects and multi-modal interactions in the samples. In each case, by adjusting the input lens to slightly modify the coupling, the spectrum was retrieved. We expect that further optimization of the fiber material components, structural design, and nano-taper profiles, enhanced spectral stability may be achieved.

### 3.4.2. Pumping at 2-μm-Wavelength

So far, dispersion and optical nonlinearities of ChG glass bulk samples were investigated. Step-index ChG fiber was produced using the characterized glasses. GVD of the nanotapers at $\lambda = 1.55$ and 2 μm and optical nonlinearities at $\lambda = 1.55$ μm were studied. Large index contrast between the core and cladding materials leads to strong mode-confinement, and enhances the optical nonlinearities in the nanotapers. Furthermore strong mode-confinement enables dispersion engineering by enhancing the waveguide-GVD. High nonlinearity and GVD-control in the nanotapers, introduce them as good options for MIR-SCG application.

Material dispersion in ChGs decreases with wavelength. For instance, for the G2 glass which the fiber core, material GVD at 1.95 μm is about 17% less than 1.55 μm. On the other hand, waveguide GVD becomes larger for longer wavelengths. Hence overcoming the material dispersion and reaching to the zero dispersion or anomalous is easier. This is our motivation to pump the nanotapers with longer wavelength sources. We thus performed some experiments using fsec-Thulium-fiber-lasers.

In the first experiment a 6.8-cm-long nanotaper with $d_c^{min}$=250 nm was pumped with 450-fs pulses from a home-made thulium fiber laser (made by LPL group in CREOL). The repetition rate of the laser was 58 MHz. we could generate spectral broadening from 0.9 μm to 3.2 μm when the input average power was 250 mW (Fig. 21-b). Unlike the SC generated by 1550 nm pump-wavelength, the

broadening here remained relatively stable in time. Higher input average power would damage the sample.

Before pumping with 2-µm-pulses, the setup was aligned with a 1.55-µm CW diode laser. The transmission through the sample was measured to be 25% for 1.55-µm-wavelength (including the 21.6% Fresnel loss on each facet), while it dropped to about 5% for 2-µm-wavelength pump. The reason large optical loss in the polymer jacket at MIR since some of the optical power enters the polymer at very narrow sections of the taper (Fig. 9-b). The schematic of the MIR spectral measurement is presented in Fig. 21-a. Two OSAs could cover the spectral range from visible to 2.4 µm; to use the OSAs, the beam after exiting the nanotaper was collimated by a 6.2-mm-focal length Aspherical lens, and coupled into a single mode fiber by means of a fiber collimator. Longer wavelengths were measured by a PbSe detector connected to a monochromator and lock-in amplifier. The signal was modulated by a chopper before entering the monochromator. A long-pass-filter was also placed on the beam path to avoid overlapping of the long-wavelengths with the diffracted short-wavelengths in the monochromator.

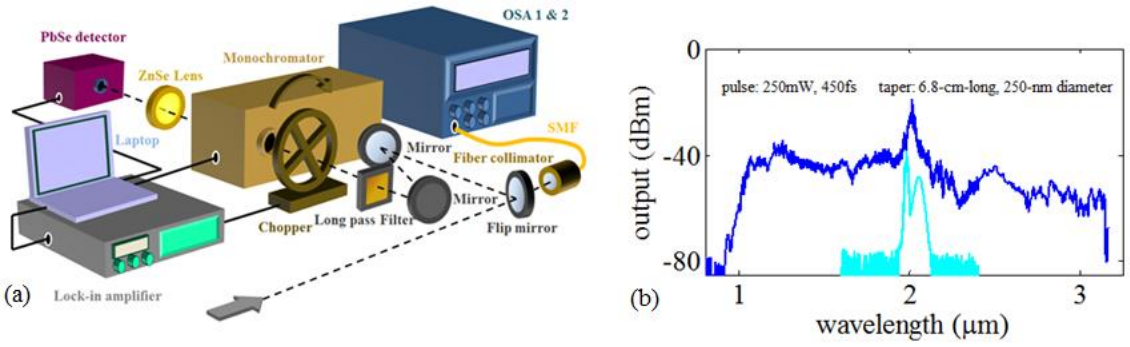


Fig. 21. (a) Schematic of the optical setup for MIR spectral measurement; shorter wavelengths from visible to 2.4 µm are measured by means of two OSAs, longer wavelengths are modulated by a chopper, routed through a monochromator and measured by a PbSe detector connected to a lock-in amplifier. A long-pass-filter is placed on the beam path to avoid overlapping of the long-wavelengths with the diffracted short-wavelengths in the monochromator. (b) Measured continuum generated from a 6.8-cm-long nanotaper with $d_c^{min}$=250 nm, pumped at 2 µm by 450-fs pulses, with an average power of 250 mW and 58-MHz repetition rate.

In the second experiment, a 7-cm-long nanotaper with $d_c^{min}$=400 nm was pumped with sub-100-fs pulses at 80 MHz. For 80-mW-input average power the SC bandwidth was spanning over an octave from 1.3 µm to 2.6 µm. As the input power was increased, the continuum edge on the right side extended more towards longer wavelengths; but on the left side, the power was transferred to a peak centering at 1 µm (Fig. 22). The intensity drop at 2.7 µm is due to water absorption coming from moisture in the chalcogenide glass. Optical transmission through the nanotaper was measured to be 20% at λ = 1.55 µm (including the 21.6% Fresnel loss on each facet); however it dropped to about 4% when the wavelength was switched to 2 µm and the average power was 50 mW. When the power was raised to 100 mW, the transmission decreased to about 1.5-2%. This is due to more broadening in long-wavelength side of the continuum and consequently more absorption in the polymer jacket of the fiber (Fig. 9-b).

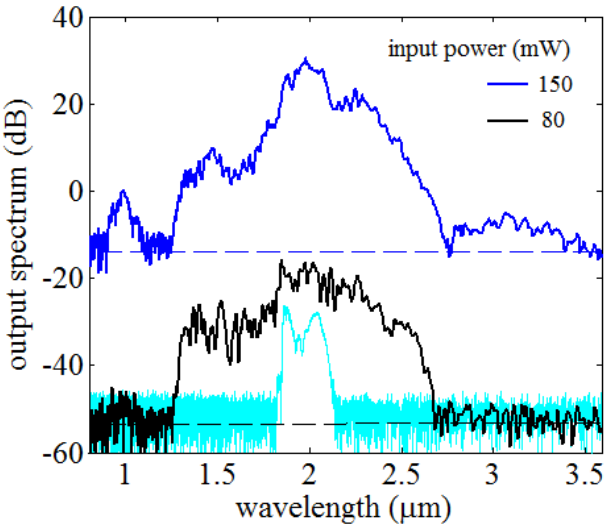


Fig. 22. Measured continuum generated from a 7-cm-long nanotaper with $d_c^{min}$=400 nm, pumped by sub-100-fs pulses, operating at 80-MHz repetition rate. The dashed lines show the noise level of detector. The spectral measurement was by means of an OSA (up to 1700 nm) and an FTIR and liquid nitrogen detector for longer wavelengths.

In conclusion, high nonlinearity, wide transparency window, capability of code confining and GVD-control along with the unique mechanical properties of our nanotapers, introduce them as good platforms for MIR nonlinear applications such as SCG. We demonstrate it by simulations and

experiments and could generate more than octave MIR-SC by pumping the nanotapers with several optical sources at 1.55 μm and 2 μm wavelengths.

# CHAPTER 4
# PARTICLE FABRICATION BY PLATEAU-RAYLEIGH CAPILLARY INSTABILITY IN MULTI-MATERIAL OPTICAL FIBERS

As a descending water jet accelerates, it narrows and ultimately breaks up into droplets, a common everyday observation captured by the Plateau-Rayleigh (PR) capillary Instability [92–95]. Two competing classes of force give rise to this instability: (1) surface tension that minimizes the surface area and disrupts the jet and (2) inertia [96], viscous dissipation forces [97], or visco-elastic forces [98] that maintain it. Hydrodynamic instabilities have recently become particularly pertinent to optical fiber fabrication with the development of photonic crystal fibers containing air holes [99] and multi-material fibers where distinct solid materials are co-drawn to form novel fiber sensors [50, 100] and actuators [101]. In contrast to traditional optical fibers where the core and cladding are virtually the same material, these novel fibers involve heterogeneous interfaces that are susceptible to instability growth during processing at elevated temperatures and low viscosity. For example, it has been established that scattering from frozen surface capillary waves is the dominant source of optical transmission loss in photonic crystal fibers [102, 103] and that fluid instabilities limit the reduction in feature size in multi-material fibers [104, 105] Surface-tension-driven instabilities, which dominate at large surface curvature, are consequently expected to determine the smallest transverse size of an axially continuous feature in a multi-material fiber. We present here the first observation of the PR capillary instability in a multi-material fiber at the core-cladding interface. We observe a wide gamut of dynamical fluid phenomena in the fibers such as droplet pinch-off, growth of periodic droplet arrays, and inter-droplet satellite and sub-satellite formation. We also develop a quasi-static extension of Tomotika's linear stability analysis [106] as a theoretical framework for our findings.

We use fiber tapering [107, 108] to study the effect of scale reduction and thermal treatment on multi-material fiber stability. The fiber is inserted in a heating zone for a fixed time interval before both fiber ends are pulled symmetrically in opposite directions (Fig. 23). The three controllable

tapering parameters (inset of Fig. 23-a) are (1) temperature T, which determines the viscosity, (2) tapering distance *l*, which determines the size reduction, and (3) tapering speed *v*, which determines the dwelling time in the heating zone. The fiber used in this study consists of a chalcogenide glass ($As_2Se_3$) core and PES cladding (Fig. 23-b). A typical taper is shown in Fig. 23-c. The initially continuous core has evolved into a periodic string of droplets in the tapered section (Fig. 23-d). This highly robust observation is a manifestation of the PR capillary instability culminating in fiber-core breakup, as we proceed to demonstrate. The full process is shown in Fig. 23-e with increasing T (at fixed *v* and *l*). At lower T, the viscosity is large (Fig. 23-f), and the core remains intact. As T increases, the viscosity drops and surface tension overcomes the inertial viscous force, leading to instability growth until droplets are formed.

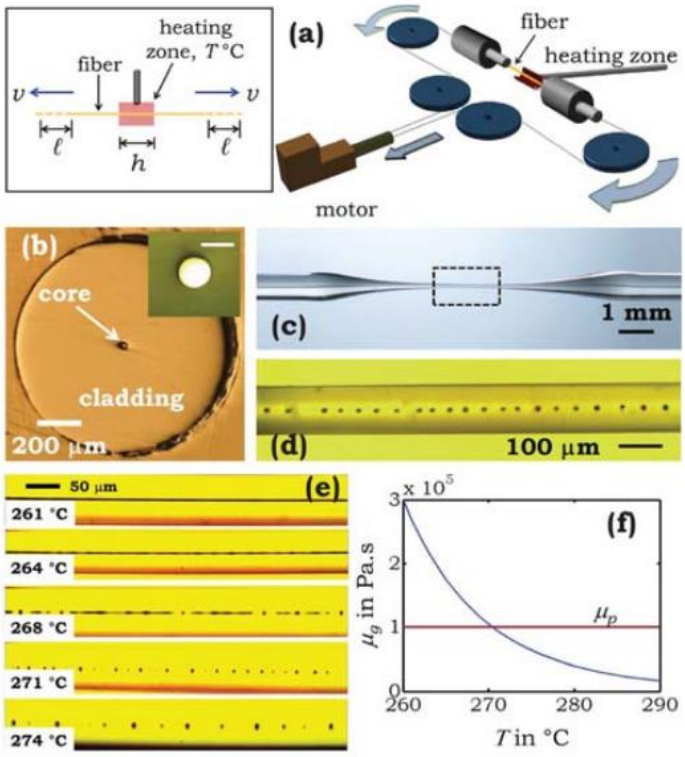


Fig. 23. (a) Tapering setup. Inset shows the tapering parameters. (b) Optical micrograph of a fiber cross section. Inset shows a magnified image of the core (scale bar is 20 μm). (c) A typical fiber taper side view. (d) Magnified side view image of the taper center (corresponding to the dotted box in (c)) showing the broken core. (e) Optical micrographs of the fiber tapers side view produced at different T (*v*=0.5mm/s and *l*=15 mm) showing different stages of the core breakup driven by the PR capillary instability. (f) Glass viscosity $\mu_g$ as a function of T.

We first examine the effect of static fiber heating ($v$=0) on the core stability. Since the result is "frozen" in the fiber, we can monitor the details of the instability growth. We heat identical fibers for progressively longer intervals, dissolve the cladding using an organic solvent [104], and obtain scanning electron microscope (SEM) micrographs of the core (Fig. 24-a). Although the PR instability is initiated through thermodynamic fluctuations at the core-cladding interface [102], single instability wavelengths are favored by the process and grow without bound resulting in core breakup [106]. A shallow sinusoidal modulation first appears at the interface (Fig. 24-b) and the modulation depth increases (Fig. 24-c) until droplets form (Fig. 24-d). A bridge connects the "mother" droplets until pinch-off, at which point the droplets detach leaving a satellite in the middle (Fig. 24-e) [109]. The satellite in turn undergoes the same capillary instability, breaking up into sub-satellites at a smaller scale (Fig. 24-f). This fractal process continues at progressively smaller scales down to a fourth generation as shown in Fig. 24-g (a total of 9 satellite droplets between mother droplets) [109].

We measured the breakup time $\tau_B$ (heating time needed until core breakup) in the static case and find that it depends inversely on T (Fig. 24-a). To analyze these results quantitatively we adopt the linear stability analysis of Tomotika [106] which was developed for a stationary viscous incompressible fluid thread embedded in an unbound viscous fluid. The details of our analysis are presented in ref. [36].

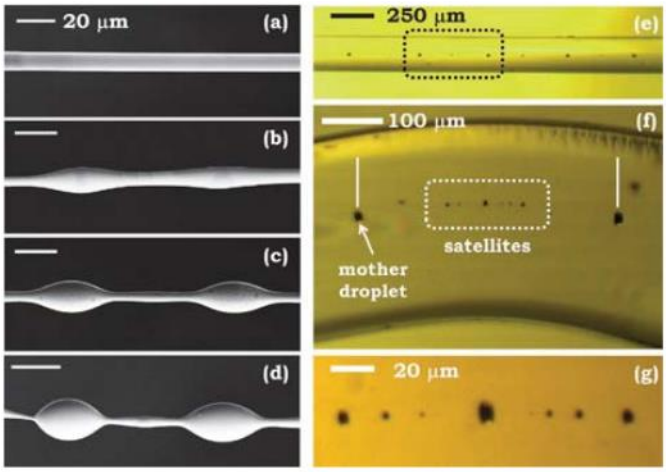


Fig. 24. (a)–(d) SEM micrographs of the fiber core at different stages of the PR instability during static heating at 287° C. Scale bars are all 20 μm. (e) Optical micrograph of the fiber after core breakup. (f) A single period corresponding to the dotted box in (e). In order to make the satellites visible, the fiber is squeezed between two microscope slides. (g) Magnified image of the satellites and sub-satellites corresponding to the dotted box in (f).

In order to describe the breakup process during tapering, we adopt a quasi-static model that decouples the instability growth from the tapering dynamics [36]. This may be justified by the difference in time scales of the two processes: the slow breakup and the rapid variation in size during tapering. This model, despite its simplicity, yields results in good agreement with our observations. The taper diameter at time t after start of tapering is $D(t,v) = D_i \exp\{vt/h\}$, where the initial core diameter at t=0 is $D_i$=10 μm and h is the length of the heating zone (7.5mm). This formula is derived utilizing geometric considerations and simplifying but reasonable physical assumptions: (1) conservation of volume, (2) a uniform spatial distribution of temperature in the heating zone, and (3) the material exiting the heating zone cools down immediately.

When we increase *l* [*v*=1 mm/s, T=285 °C; Fig. 25-c], the core remains intact until *l*=21 mm, after which it breaks up, and further elongation increases the droplet separation. Next consider the effect of *v* [*l*=23 mm, T=285 °C; Fig. 25-d]. At high *v*, the dwelling time in the heating zone may be less than $\tau_B$ and the core remains intact. At lower *v*, the fiber dwells longer, thus having the opportunity to reach $\tau_B$ and hence breaks up. Consequently, tapering at high speeds allows us to reach smaller-diameter cores before breakup. Finally, consider the effect of T [*v*=1 mm/s, *l*=23 mm; Fig. 25-e]. At low T, the viscosity of the core is relatively large and the core remains intact. As T

increases, the PR instability grows until droplets are formed and the period increases with T. The quality of the fit in Fig. 25-e is less than in Fig. 25-c and Fig. **25**-d which show the effect of kinematic parameters *v* and *l*. Our linear model does not consider the strongly nonlinear processes that take place during pinch-off and droplet breakup. Nevertheless, since these later stages occur at much faster time scales than that of the initial instability development, it is expected that our model will still provide a reasonable prediction of period of breakup.

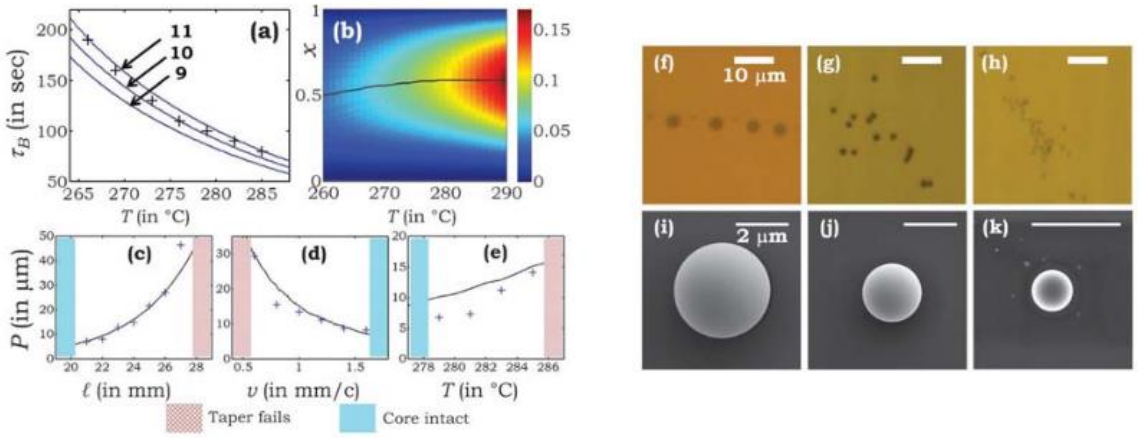


Fig. 25. (a) Dependence of the instability growth time $\tau_B$ on temperature T during static heating. We calculate and plot $\tau_B$ over the same temperature range for D=9, 10, and 11 µm. (b) Calculated instability rate ($1/\tau_B$) as a function of T and x. The black line shows the highest instability rate as a function of temperature, thus identifying $x_m$. (c)–(e) Effect of tapering parameters on core breakup period $P_B$: (c) l, (d) v, and (e) T. Continuous curves are theoretical fits and "+" are data points. (f)–(h) Optical micro-graphs of glass particles with prescribed sizes obtained after dissolving the polymer cladding. Scale bars are all 10 µm. (i)–(k) SEM micrographs of single particles corresponding to (f)–(h), respectively. Scale bars are all 2 µm.

The process described here offers an unconventional top-down approach to fabricating solid micro-structures with tunable size. Particles of prescribed size are produced in two steps: the fiber is tapered at high speed to reach an intact core-diameter D, after which it is heated to induce breakup into spheres with diameter. In general if the core diameter is D at breakup, then the particle diameter is 2D.

Temperature and tapering rate may be used as parameters to control the onset of the Plateau-Rayleigh instability, thus indirectly the resulting particle diameter. To demonstrate size control, we produce particles at three different sizes: 5, 3 and 1 µm (Figs. 24-f–24-k). Using dynamic light

scattering (DLS) measurements we have established that the standard deviation of the particle size dispersion is typically 10% of the mean particle size. Furthermore, this approach is amenable to a wide range of materials that may be included in multi-material fibers [50, 100, 101] where the instability dynamics are dominated by viscosity and surface tension. Examples of such materials include soft glasses and thermoplastic polymers [50]. Moreover, since the process starts from a macroscopic preform, it may be possible to obtain particles of complex structure by constructing the preform with the prescribed structure. In summary, we have reported the observation of the PR capillary instability in multi-material optical fiber cores during tapering, leading to breakup of the core into spherical droplets. A theoretical model was developed that determines the effect of tapering parameters on the core stability. This setting offers a new playground for micro-scale fluid dynamics extending it into new geometries and materials. The physical process described here is an unconventional top-down approach to the fabrication of micro-structures from a variety of materials. Using this approach we have demonstrated control over the particle diameter in the 1–20 μm range. It seems possible that this technique may be extended to the fabrication of both larger particles and smaller nanoparticles from a variety of materials that can be processed by thermal drawing. This surface-tension-driven instability results in extremely smooth particle surfaces, making them potentially useful in photonics applications as optical micro-resonators.

# APPENDIX A
# GLASS FABRICATION AND PREFORM EXTRUSION

Bulk glass samples are prepared from commercial glass (Amorphous Materials, Inc.) by melt-quenching [54, 110]. The as-purchased glass (typically 10–150 g) is crushed into small pieces with average size <10 mm and loaded into a silica ampoule, which is evacuated (10−4 Pa) and sealed with a propane-oxygen flame. The ChG is melted in a rocking furnace at 900 – 950 ◦C for 12 hours, quenched in cold water, and then annealed near the glass-transition temperature for 2–5 hours to produce 10-mm and 30-mm-diameter glass rods for bulk measurements and fiber preform extrusion, respectively. Three glass compositions were investigated: G1, $As_2Se_3$; G2, $As_2Se_{1.5}S_{1.5}$; and G3, $As_2S_3$. G1 and G3 were directly re-melted from AMTIR-2 and AMTIR-6 glasses [111], respectively, while G2 was synthesized by mixing G1 and G3. Finally, the annealed 10-mm- and 30-mm-diameter glass rods were cut and polished into discs for further measurements and for extrusion, respectively.

The billets used in extruding the preforms were prepared by vertically stacking discs of the appropriate materials. Three 30-mm-diameter 15-mm-thick discs are vertically stacked in a cylindrical billet: the bottom disc is the polymer, the second disc is the cladding ChG, and the top disc is the core ChG. The polymer discs were prepared by thin-film-rolling technology [55, 112]. The billet is then heated in a stainless steel sleeve and extruded under pressure through a 12-mm-diameter circular die. The extruded preform consists of nested cylindrical shells with the bottom (top) disc in the billet corresponding to the outermost (innermost) layer. A thin polymer film (75-μm-thick PES) was rolled around a section of the extruded multimaterial preform and thermally consolidated under vacuum to produce a preform with a thicker polymer jacket, which – in turn – we draw into fibers.

# APPENDIX B
# ZSCAN MEASUREMENT

The nonlinear refractive indices $n_2$ of the ChGs we make use of here were measured at $\lambda$=1.55 μm by the Z-scan technique [81] using ≈100 fs (FWHM) pulses generated by an OPA/OPG (Light Conversion Ltd. model TOPAS-C) pumped by a regenerative Ti:Sapphire amplifier (Clark-MXR CPA 2010) operating at a 1 kHz repetition rate, delivering ≈1 mJ pulses at 780 nm. To verify the setup accuracy and calibrate the input-beam spot size and pulse duration, open-aperture Zscans were performed on the bulk semiconductor GaAs [84], for which the two-photon absorption spectrum is theoretically calculated and experimentally verified (14 cm/GW) [85]. Closed-aperture Zscan measurements are also calibrated against fused silica with documented $n_2$ values ($n_2^{quartz}$ $=2.6\times10^{-16}cm^2/W$) [113]. Due to sample inhomogeneity, surface irregularities, or non-parallel facets, a linear transmittance change of ~20% was observed using a small spot size and weak probe beam scanning across the sample; therefore, initial Z-scan traces showed a large background. To obtain the Z-scan background, a low-energy Zscan (0.3–0.5 nJ) was performed, restricted by the sensitivity of the Ge detectors, prior to higher energy Zscans. All Z-scan curves at higher energy levels are then obtained by dividing the normalized raw data with this low-energy scan to cancel the background. Due to relatively large n2 values of the samples, a small closed-aperture signal, estimated to be about 4% – 5% from peak to valley, was already induced but buried in the background signal. Given the fact that only n2 and no higher order nonlinearity is involved in nonlinear refraction, the energy of the "background-free" Zscan curves [shown in Fig. 13-a] is estimated by subtracting the actual energy from the background scan energy.

# APPENDIX C
# SPECTRAL BROADENING SIMULATIONS

Simulations of the nonlinear propagation dynamics of ultrafast pulses along nanotapers with axially varying diameter were carried out using the generalized nonlinear Schrödinger equation (GNLSE) [74] integrated via the symmetrized split-step method [48]. In our simulations, we included in the GNLSE terms that account for the following effects: (1) wavelength-dependent linear loss, (2) GVD, (3) SPM, (4) Raman response, and (5) self-steepening. Some of these effects depend on the core diameter dc and, hence, vary along the nanotaper axis z. A linearly polarized transform-limited Gaussian pulse (discretized on a lattice of $2^{15}$ points) is launched in the fundamental mode. To ensure convergence we adaptively changed the axial step size to restrict the nonlinear SPM phase shift to 0.001 rad/step [19]. The parameters used in the simulations were chosen as follows:

(1) Linear spectral losses were determined by FTIR transmission measurements [15].

(2) The GVD used was the sum of the material GVD for the core ChG (measured in bulk [15]) and the waveguide GVD calculated in COMSOL using the refractive indices in Table 1 and the axial profiles of the nanotaper samples shown in Fig. 9-a. We assumed that the material GVD varied linearly between $\lambda$=1.55 and 2 μm; higher-order dispersion terms were neglected.

(3) The SPM term depends on mode confinement (related to $d_c$ and the core-to-cladding index contrast) and the nonlinear indices $n_2$ for the core and cladding ChGs. We calculated the axially varying fundamental mode field distribution along the nanotaper using COMSOL (at $\lambda$=1.55 μm) and used the bulk $n_2$ values reported above. At the input, $\gamma = 0.23\ W^{-1}m^{-1}$ where $d_c = 10$ μm, which subsequently increases to $\gamma = 4.41$, 11.72, and 19.95 $W^{-1}m^{-1}$ at $d_c = 2$ μm, 1 μm, and 250 nm, respectively.

(4) The Raman response function and Raman strength coefficient for As2Se1.5S1.5 are taken to be an average of those for As2Se3 [90] and As2S3 [91].

(5) The self-steepening is modeled to first order using an optical-shock time constant $\tau_{s=} 1/\omega_o$ [74], where $\omega_o$ is the optical frequency corresponding to the central wavelength.

The integration of the parametric four-wave-mixing gain over the length of nanotapers was found not to play a significant role in the spectral broadening, so four-wave mixing was neglected in our calculations.

# REFERENCES


[1] J. S. Sanghera, I. D. Aggarwal, L. B. Shaw, L. E. Busse, P. Thielen, V. Nguyen, P. Pureza, S. Bayya, and F. Kung, J. Optoelectron. Adv. M. **3**, 627 (2001).

[2] A. Zakery and S. R. Elliott, Optical Nonlineartities in Chalcogneide Glasses and their Applications (Springer, 2007).

[3] G. Lenz, J. Zimmermann, T. Katsufuji, M. E. Lines, H. Y. Hwang, S. S. alter, R. E. Slusher, S.-W. Cheong, J. S. Sanghera, and I. D. Aggarwal, Opt. Lett. **25**, 254 (2000).

[4] B. J. Eggleton, T. D. Vo, R. Pant, J. Schroder, M. D. Pelusi, D. Y. Choi, S. J. Madden, and B. L. Davies, Laser & Photon. Rev. **6**, 97 (2012).

[5] Y. Xu, H. Zeng, G. Yang, G. Chen, Q. Zhang, and L. Xu, Opt. Mater. **31**, 75 (2008).

[6] G. Qin, X. Yan, C. Kito, M. Liao, T. Suzuki, A. Mori, and Y. Ohishi, J. Appl. Phys. **107**, 043108 (2010).

[7] P. Domachuk, N. A. Wolchover, M. Cronin-Golomb, A. Wang, A. K. George, C. M. B. Cordeiro, J. C. Knight, and F. G. Omenetto, Opt. Express **16**, 7161 (2008).

[8] O. P. Kulkarni, V. V. Alexander, M. Kumar, M. J. Freeman, M. N. Islam, F. L. Terry, M. N. Jr., and A. Chan, JOSA B **28**, 2486 (2011).

[9] Z. Chen, A. J. Taylor, and A. Efimov, Opt. Express **17**, 5852 (2009).

[10] R. R. Gattass, L. B. Shaw, V. Nguyen, P. Pureza, I. D. Aggarwal, and J. S. Sanghera, "All-fiber chalcogenide-based mid-infrared supercontinuum source," Opt. Fiber Technol. **18**, 345 (2012).

[11] J. S. Sanghera, L. B. Shaw, and I. D. Aggarwal, "Applications of chalcogenide glass optical fibers," C. R. Chimie **5**, 873 (2002).

[12] L. B. Shaw, P. A. Thielen, F. H. Kung, V. Q. Nguyen, J. Sanghera, and I. Aggarwal, "IR supercontinuum generation in As–Se photonic crystal fiber," Proc. Advanced Solid State Photonics p. TuC5 (2005).

[13] C. Florea, L. Busse, J. Sanghera, B. Shaw, and I. R. Aggarwal, "A simple phenomenological study of photodarkening in As2S3 glasses," Opt. Mater. **34**, 1389–1393 (2012).

[14] I. V. Fekeshgazi, K. V. Mai, N. I. Matelesko, V. M. Mitsa, and E. I. Borkach, “Structural transformations and optical properties of As2S3 chalcogenide glasses, ” Semiconductors **39**, 951–954 (2005).

[15] S. Shabahang, G. Tao, J. J. Kaufman, and A. F. Abouraddy, “Dispersion characterization of chalcogenide bulk glass, composite fibers, and robust nanotapers, ”J. Opt. Soc. Am. B **30**, 2498–2506 (2013).

[16] L. B. Shaw, R. R. Gattass, J. S. Sanghera, and I. D. Aggarwal, “All-fiber mid-IR supercontinuum source from 1.5 to 5 μm, ” Proc. SPIE 7914, 79140P (2011).

[17] M. Duhant, W. Renard, G. Canat, T. N. Nguyen, F. Smektala, J. Troles, Q. Coulombier, P. Toupin, L. Brilland, P. Bourdon, and G. Renversez, “Fourth-order cascaded Raman shift in AsSe chalcogenide suspended-core fiber pumped at 2 μm,” Opt. Lett. **36**, 2859–2861 (2011).

[18] M. El-Amraoui, G. Gadret, J. C. Jules, J. Fatome, C. Fortier, F. Désévédavy, I. Skripatchev, Y. Messaddeq, J. Troles, L. Brilland, W. Gao, T. Suzuki, Y. Ohishi, and F. Smektala, “Microstructured chalcogenide optical fibers from As2S3 glass: towards new IR broadband sources,” Opt. Express **18**, 26655–26665 (2010).

[19] S. Shabahang, M. P. Marquez, G. Tao, M. U. Piracha, D. Nguyen, P. J. Delfyett, and A. F. Abouraddy, “Octave-spanning infrared supercontinuum generation in robust chalcogenide fiber nano-tapers using picosecond pulses,” Opt. Lett. **37**, 4639–4641 (2012).

[20] D. D. Hudson, S. A. Dekker, E. C. Mägi, A. C. Judge, S. D. Jackson, E. Li, J. S. Sanghera, L. B. Shaw, I. D. Aggarwal, and B. J. Eggleton, “Octave spanning supercontinuum in an As2S3 taper using ultralow pump pulse energy,” Opt. Lett. **36**, 1122–1124 (2011).

[21] J. M. Dudley, G. Genty, and S. Coen, “Supercontinuum generation in photonic crystal fiber,” Rev. Mod. Phys. **78**, 1135–1184 (2006).

[22] L. Brilland, F. Smektala, G. Renversez, T. Chartier, J. Troles, T. N. Nguyen, N. Traynor, and A. Monteville, “Fabrication of complex structures of holey fibers in chalcogenide glass,” Opt. Express **14**, 1280–1285 (2006).

[23] K. M. Mohsin, M. S. Alam, D. M. N. Hasan, and M. N. Hossain, “Dispersion and nonlinearity properties of a chalcogenide As2Se3 suspended core fiber,” Appl. Opt. **50**, E102–E107 (2011).

[24] M. Liao, X. Yan, G. Qin, C. Chaudhari, T. Suzuki, and Y. Ohishi, “Controlling the chromatic dispersion of soft glass highly nonlinear fiber through complex microstructure,” J. Non-Cryst. Solids **356**, 2613–2617 (2010).

[25] T. A. Birks, W. J. Wadsworth, and P. St. J. Russell, “Supercontinuum generation in tapered fibers,” Opt.Lett. **25**, 1415–1417 (2000).

[26] E. C. Mägi, L. B. Fu, H. C. Nguyen, M. R. E. Lamont, D. I. Yeom, and B. J. Eggleton, "Enhanced Kerr nonlinearity in sub-wavelength diameter As2Se3 chalcogenide fiber tapers," Opt. Express **15**, 10324–10329 (2007).

[27] L. B. Fu, M. D. Pelusi, E. C. Mägi, V. G. Ta'eed, and B. J. Eggleton, "Broadband all-optical wavelength conversion of 40 Gbit/s," Electron. Lett. **44**, 44–46 (2008).

[28] F. Luan, J. V. Erps, M. Pelusi, E. Mgi, T. Iredale, H. Thienpont, and B. Eggleton, Electron. Lett. **46**, 223 (2010).

[29] W. Gao, M. Liao, X. Yan, C. Kito, T. Kohoutek, T. Suzuki, M. E. Amraoui, J. C. Jules, G. Gadret, F. Désévédavy, F. Smektala, and Y. Ohishi, "Visible light generation and its influence on supercontinuum in chalcogenide As2S3 microstructured optical fiber," Appl. Phys. Express **4**, 102601 (2011).

[30] N. Granzow, S. Stark, M. Schmidt, A. Tverjanovich, A. L. Wondraczek, and P. Russell, "Supercontinuum generation in chalcogenide-silica step-index fibers, " Opt. Express **19**, 21003–21010 (2011).

[32] C. Baker and M. Rochette, "High nonlinearity and single-mode transmission in tapered multimode As2Se3-PMMA fibers," IEEE Photon. J. **4**, 960–969 (2012).

[33] C. Chaudhari, M. Liao, T. Suzuki, and Y. Ohishi, J. Lightwave Technol. **30**, 2069 (2012).

[34] G. Tao, S. Shabahang, E.-H. Banaei, J. J. Kaufman, and A. F. Abouraddy, "Multimaterial preform co-extrusion for robust chalcogenide optical fibers and tapers," Opt. Lett. **37**, 2751–2753 (2012).

[35] J. S. Sanghera, L. B. Shaw, and I. D. Aggarwal, IEEE J. Sel. Topics in Quantum Elect. **15**, 114 (2009).

[36] S. Shabahang, J. J. Kaufman, D. S. Deng, and A. F. Abouraddy, "Observation of the Plateau-Rayleigh capillary instability in multi-material optical fibers," Appl. Phys. Lett. **99**, 161909 (2011).

[37] G. Brambilla, F. Xu, P. Horak, Y. Jung, F. Koizumi, N. P. Sessions, E. Koukharenko, X. Feng, G. S. Murugan, J. S. Wilkinson, and D. J. Richardson, "Optical fiber nanowires and microwires: fabrication and applications," Adv. Opt. Photon. **1**, 107–161 (2009).

[38] J. J. Kaufman, G. Tao, S. Shabahang, D. S. Deng, Y. Fink, and A. F. Abouraddy, "Thermal drawing of high-density macroscopic arrays of well-ordered sub-5-nm-diameter nanowires," Nano Lett. **11**, 4768–4773 (2011).

[39] J. J. Kaufman, G. Tao, S. Shabahang, E.-H. Banaei, D. S. Deng, X. Liang, S. G. Johnson, Y. Fink, and A. F. Abouraddy, "Structured spheres generated by an in-fibre fluid instability," Nature **487**, 463–467 (2012).

[40] L. G. Cohen, J. Lightwave Technol. **3**, 958 (1985).

[41] V. Page and L. Chen, Opt. Commun. **265**, 161 (2006),

[42] D. Ouzounov, D. Homoelle, W. Zipfel, W. W. Webb, A. L.Gaeta, J. A.West, J. C. Fajardo, and K.W. Koch, Opt. Commun. **192**, 219 (2001).

[43] C. Lin, L. G. Cohen, W. G. French, and H. M. Presby, IEEE J. Quant. Electron. **16**, 33 (1980).

[44] B. Costa, D. Mazzoni, M. Puleo, and E. Vezzoni, IEEE Trans. Microw. Theory Techn. **18**, 1497 (1982).

[45] T. M. Kardas and C. Radzewicz, Opt. Commun. **282**, 4361 (2009).

[46] N. K. Berger, B. Levit, and B. Fischer, Opt. Commun. **283**, 3953 (2010).

[47] P. Merritt, R. P. Tatam, and D. A. Jackson, "Interferometric chromatic dispersion measurements on short lengths of mono-mode optical fiber," J. Lightwave Technol. **7**, 703–716 (1989).

[48] G. P. Agrawal, Nonlinear Fiber Optics, 3rd ed. (Academic Press, New York, (2001).

[49] G. Delaizir, J.-S. Sangleboeuf, E. A. King, Y. Gueguen, X. H. Zhang, C. Boussard-Pledel, B. Bureau, and P. Lucas, "Influence of ageing conditions on the mechanical properties of Te-As-Se fibers," J. Phys. D **42**, 095405 (2009).

[50] R. E. Slusher, G. Lenz, J. Hodelin, J. Sanghera, L. B. Shaw, and I. D. Aggarwal, "Large Raman gain and nonlinear phase shifts in high-purity As2Se3 chalcogenide fibers," J. Opt. Soc. Am. B **21**, 1146–1155 (2004).

[51] I. Walmsley, L. Waxer, and C. Dorrer, "The role of dispersion in ultrafast optics," Rev. Sci. Instrum. **72**, 1–29 (2001).

[52] J. M. Dudley and J. R. Taylor, eds., Supercontinuum Generation in Optical Fibers (Cambridge University, 2010).

[53] B. Dabas and R. Sinha, "Dispersion characteristic of hexagonal and square lattice chalcogenide As2Se3 glass photonic crystal fiber," Opt. Commun. **283**, 1331–1337 (2010).

[54] S. A. Ray Hilton, Chalcogenide Glasses for Infrared Optics (McGraw-Hill, 2009).

[55] G. Tao, A. M. Stolyarov, and A. F. Abouraddy, "Multimaterial fibers," I. J. Appl. Glass Sci. **3**, 349–368 (2012).

[56] S. W. Haruna, K. S. Limb, and H. Ahmad, "Investigation of dispersion characteristic in tapered fiber," Laser Phys. **21**, 945–947 (2011).

[57] S. D. Le, D. M. Nguyen, M. Thua, L. Bramerie, M. C. e Silva, K. Lenglé, M. Gay, T. Chartier, L. Brilland, D. Méchin, P. Toupin, and J. Troles, "Efficient four-wave mixing in an ultra-highly nonlinear suspended-core chalcogenide As38Se62 fiber," Opt. Express **19**, B653–B660 2011).

[58] G. Imeshev and M. E. Fermann, "230-kW peak power femtosecond pulses from a high power tunable source based on amplification in Tm-doped fiber," Opt. Express **13**, 7424–7431 (2005).

[59] M. A. Solodyankin, E. D. Obraztsova, A. S. Lobach, A. I. Chernov, A. V. Tausenev, V. I. Konov, and E. M. Dianov, "Mode-locked 1.93 μm thulium fiber laser with a carbon nanotube absorber," Opt. Lett. **33**, 1336–1338 (2008).

[60] K. Kieu and F. W. Wise, "Soliton thulium-doped fiber laser with carbon nanotube saturable absorber," IEEE Photon. Technol. Lett. **21**, 128–130 (2009).

[61] T. S. McComb, R. A. Sims, C. C. C. Willis, P. Kadwani, V. Sudesh, L. Shah, and M. Richardson, "High-power widely tunable thulium fiber lasers," Appl. Opt. **49**, 6236–6238 (2010).

[62] F. Haxsen, D. Wandt, U. Morgner, J. Neumann, and D. Kracht, "Pulse characteristics of a passively mode-locked thulium fiber laser with positive and negative cavity dispersion," Opt. Express **18**, 18981–18988 (2010).

[63] W. Burckhardt, "Refractive index and dispersion of glasses with different degrees of linking," J. Non-Cryst. Solids **50**, 173–182 (1982).

[64] W. S. Rodney, I. H. Malitson, and T. A. King, "Refractive index of arsenic trisulfide," J. Opt. Soc. Am. **48**, 633–636 (1958).

[65] J. Hu, C. R. Menyuk, L. B. Shaw, J. S. Sanghera, and I. D. Aggarwal, "Computational study of 3–5 μm source created by using supercontinuum generation in As2S3 chalcogenide fibers with a pump at 2 μm," Opt. Lett. **35**, 2907–2909 (2010).

[66] N. Carlie, J. N. C. Anheier, H. A. Qiao, B. Bernacki, M. C. Phillips, L. Petit, J. D. Musgraves, and K. Richardson, "Measurement of the refractive index dispersion of As2Se3 bulk glass and thin films prior to and after laser irradiation and annealing using prism coupling in the near- and mid-infrared spectral range," Rev. Sci. Instrum. **82**, 053103 (2011).

[67] M. Asobe, T. Kanamori, and K. Kubodera, "Applications of highly nonlinear chalcogenide glass fibers in ultrafast all-optical switches," IEEE J. Quantum Electron. **29**, 2325–2333 (1993).

[68] L. B. Fu, M. Rochette, V. G. Ta'eed, D. J. Moss, and B. J. Eggleton, "Investigation of self-phase modulation based optical regeneration in single mode As2Se3 chalcogenide glass fiber," Opt. Express **13**, 7637–7644 (2005).

[69] J. Fatome, C. Fortier, T. N. Nguyen, T. Chartier, F. Smektala, K. Messaad, B. Kibler, S. Pitois, G. Gadret, C. Finot, J. Troles, F. Desevedavy, P. Houizot, G. Renversez, L. Brilland, and N. Traynor, "Linear and nonlinear

characterizations of chalcogenide photonic crystal fibers," J. Lightwave Technol. **27**, 1707–1715 (2009).

[70] M. El-Amraoui, J. Fatome, J. C. Jules, B. Kibler, G. Gadret, C. Fortier, F. Smektala, I. Skripatchev, C. Polacchini, Y. Messaddeq, J. Troles, L. Brilland, M. Szpulak, and G. Renversez, "Strong infrared spectral broadening in low-loss As-S chalcogenide suspended core microstructured optical fibers, "Opt. Express **18**, 4547–4556 (2010).

[71] S. Shabahang, G. Tao, M. P. Marquez, H. Hu, T. R. Ensley, P. J. Delfyett, and A. F. Abouraddy "Nonlinear characterization of robust multimaterial chalcogenide nanotapers for infrared supercontinuum generation" J. Opt. Soc. Am. B **31**, 450-457 (2014).

[72] T. Kanamori, Y. Terunuma, S. Takahashi, and T. Myashita, "Chalcogenide glass fibers for mid-infrared transmission," J. Lightwave Technol. **2**, 607–613 (1984).

[73] N. J. Pitt, G. S. Sapsford, T. V. Clapp, R. Worthington, and M. G. Scott, "Telluride glass fibres for transmission in the 8-12 micrometres waveband," Proc. SPIE **618**, 124–129 (1986).

[74] J.M.Dudley, G.Genty, andS.Coen, "Supercontinuum generation in photonic crystal fiber," Rev. Mod. Phys. **78**, 1135–1184 (2006).

[75] R. Ahmad and M. Rochette, "High efficiency and ultra broad-band optical parametric four-wave mixing in chalcogenide-PMMA hybrid microwires," Opt. Express **20**, 9572–9580 (2012).

[76] D.D.Hudson, S.A.Dekker, E.C.Mägi, A.C.Judge, S.D.Jackson, E. Li, J. S. Sanghera, L. B. Shaw, I. D. Aggarwal, and B. J. Eggleton, "Octave spanning supercontinuumin an As2S3 Taper using ultralow pump pulse energy," Opt. Lett. **36**, 1122–1124 (2011).

[77] D. I. Yeom, E. C. Mägi, M. R. E. Lamont, M. A. F. Roelens, L. Fu, and B. J. Eggleton, "Low-threshold supercontinuum generation in highly nonlinear chalcogenide nanowires," Opt. Lett. **33**, 660–662 (2008).

[78] F. Luan, J. Van Erps, M. D. Pelusi, E. Mägi, T. Iredale, H. Thienpont, and B. J. Eggleton, "High-resolution optical sampling of 640 Gbit/s data using dispersion-engineered chalcogenide photonic wire," Electron. Lett. **46**, 231–232 (2010).

[79] A. Marandi, C. W. Rudy, V. G. Plotnichenko, E. M. Dianov, K. L. Vodopyanov, and R. L. Byer, "Mid-infrared supercontinuum generation in tapered chalcogenide fiber for producing octave-spanning frequency comb around 3 μm," Opt. Express **20**, 24218–24225 (2012).

[80] C. W. Rudy, A. Marandi, K. L. Vodopyanov, and R. L. Byer, " Octave-spanning supercontinuum generation in situtapered As2S3 fiber pumped by a thulium-doped fiber laser," Opt. Lett. **38**, 2865–2868 (2013).

[81] M. Sheik-Bahae, A. A. Said, T. H. Wei, D. J. Hagan, and E. W. Van Stryland, "Sensitive measurement of optical nonlinearities using a single beam," IEEE J. Quantum Electron. **26**, 760–769 (1990).

[82] P. D. Olszak, C. M. Cirloganu, S. Webster, L. A. Padilha, T. R. Ensley, H. Hu, G. Nootz, D. J. Hagan, and E. W. Van Stryland, CREOL, Orlando, Florida, 32816 USA, are preparing a manuscript to be called "Three-photon absorption in direct-gap semiconductors."

[83] M. Yaman, H. E. Kondakci, and M. Bayindir, "Large and dynamical tuning of a chalcogenide Fabry–Perot cavity mode by temperature modulation," Opt. Express **18**, 3168–3173 (2010).

[84] W. C. Hurlbut, Y.-S. Lee, K. L. Vodopyanov, P. S. Kuo, and M. M. Fejer, "Multiphoton absorption and nonlinear refraction of GaAs in the mid-infrared," Opt. Lett. **32**, 668–670 (2007).

[85] M. Sheik-Bahae, D. C. Hutchings, D. J. Hagan, and E. W. Van Stryland, "Dispersion of bound electronic nonlinear refraction in solids," IEEE J. Quantum Electron. **27**, 1296–1309 (1991).

[86] J. K. Ranka, R. S. Windeler, and A. J. Stentz, Opt. Lett. **25**, 25 (2000).

[87] G. Qin, X. Yan, C. Kito, M. Liao, C. Chaudhari, T. Suzuki, and Y. Ohishi, Appl. Phys. Lett. **95**, 161103 (2009).

[88] J. S. Sanghera, I. D. Aggarwal, L. B. Shaw, C. M. Florea, P. Pureza, V. Q. Nguyen, F. Kung, and I. D. Aggarwal, J. Optoelectron. Adv. Mater. **8**, 2148 (2006).

[89] M. E. Lines, J. Appl. Phys. **55**, 4058 (1984).

[90] J. Hu, C. R. Menyuk, L. B.Shaw, J. S. Sanghera, and I. D. Aggarwal, "Maximizing the bandwidth of supercontinuum generation in As2Se3 chalcogenide fibers," Opt. Express **18**, 6722–6739 (2010).

[91] C. Xiong, E. Magi, F. Luan, A. Tuniz, S. Dekker, J. S. Sanghera, L. B. Shaw, I. D. Aggarwal, and B. J. Eggleton, "Characterization of picosecond pulse nonlinear propagation in chalcogenide As2S3 fiber," Appl. Opt. **48**, 5467–5474 (2009).

[92] J. A. F. Plateau, Acad. Sci. Brux. Mem. **16**, 3 (1843).

[93] L. Rayleigh, Proc. R. Soc. **29**, 71 (1879).

[94] L. Rayleigh, Philos. Mag. **34**, 145 (1892).

[95] J. Eggers and E. Villermaux, Rep. Prog. Phys. **71**, 036601 (2008).

[96] S. Chandrasekhar, Hydrodynamic and Hydromagnetic Stability (Clarenden, Oxford, 1961).

[97] J. Eggers, Phys. Rev. Lett. **71**, 3458 (1993).

[98] P. P. Bhat, S. Appathurai, M. T. Harris, M. Pasquali, G. H. McKinley, and O. A. Basaran, Nat. Phys. **6**, 625 (2010).

[99] P. Russell, Science **299**, 358 (2003).

[100] A. F. Abouraddy, O. Shapira, M. Bayindir, J. Arnold, F. Sorin, D. S. Hinczewski, J. D. Joannopoulos, and Y. Fink, Nature Mater. **5**, 532 (2006).

[101] S. Egusa, Z. Wang, N. Chocat, Z. M. Ruff, A. M. Stolyarov, D. Shemuly, F. Sorin, P. T. Rakich, J. D. Joannopoulos, and Y. Fink, Nature Mater. **9**, 643 (2010).

[102] P. J. Roberts, F. Couny, H. Sabert, B. J. Mangan, D. P. Williams, L. Farr, M. W. Mason, A. Tomlinson, T. A. Birks, J. C. Knight, and P. St. J. Russell, Opt. Express **13**, 236 (2005).

[103] M.-C. Phan-Huy, J.-M. Moison, J. A. Levenson, S. Richard, G. Mélin, M. Douay, and Y. Quiquempois, J. Lightwave Technol. **27**, 1597 (2009).

[104] D. S. Deng, N. D. Orf, A. F. Abouraddy, A. M. Stolyarov, J. D. Joannopoulos, H. A. Stone, and Y. Fink, Nano Lett. **8**, 4265 (2008).

[105] D. S. Deng, N. D. Orf, S. Danto, A. F. Abouraddy, J. D. Joannopoulos, and Y. Fink, Appl. Phys. Lett. **96**, 023102 (2010).

[106] S. Tomotika, Proc. R. Soc. London, Ser. A **150**, 322 (1935).

[107] T. A. Birks and Y. W. Li, J. Lightwave Technol. **10**, 432 (1992).

[108] L. Tong, R. R. Gattass, J. B. Ashcom, S. He, J. Lou, M. Shen, I. Maxwell, and E. Mazur, Nature **426**, 816 (2003).

[109] M. Tjahjadi, H. A. Stone, and J. M. Ottino, J. Fluid Mech. **243**, 297 (1992).

[110] G. Tao, H. Guo, L. Feng, M. Lu, W. Wei, and B. Peng, "Formation and properties of a noval heavy-metal chalcogenide glass doped with a igh dysprosium concentration," J. Am. Ceram. Soc. **92**, 2226–2229 (2009).

[111] http://www.amorphousmaterials.com/.

[112] A. F. Abouraddy, M. Bayindir, G. Benoit, S. D. Hart, K. Kuriki, N. Orf, O. Shapira, F. Sorin, B. Temelkuran, and Y. Fink, "Towards multimaterial multifunctional fibers that see, hear, sense and communicate," Nat. Mater. **6**, 336–347 (2007).

[113] D. Milam, "Review and assessment of measured values of the nonlinear refractive-index coefficient of fused silica," Appl. Opt. **37**, 546–550 (1998).